

## Revisiting the effects of low-concentration hydrogen in NiTi self-expandable stents

Fan SUN<sup>1\*</sup>, Laurence JORDAN<sup>1,2,3</sup>, Alexandre DA SILVA<sup>4</sup>, Frantz MARTIN<sup>5</sup>, Frédéric PRIMA<sup>1</sup>

1. PSL Research University, Chimie ParisTech - CNRS, Institut de Recherche de Chimie Paris, F-75005, Paris, France

2. Université de Paris, F-75006 Paris, France

3. AP-HP, Hospital Rothschild, F-75012 Paris, France

4. Institut Galien, Université Paris-Sud, Faculté de Pharmacie, F-92296 Châtenay-Malabry, France

5. Université Paris-Saclay, CEA, Service de la Corrosion et du Comportement des Matériaux dans leur Environnement, 91191, Gif-sur-Yvette, France

\*Corresponding author: fan.sun@chimieparistech.psl.eu

**Keywords:** NiTi self-expandable stent, hydrogen redistribution, heterogeneous deformation, stress-induced martensitic transformation, dislocation slip

### Abstract

Superelastic NiTi is widely used in self-expandable transcatheter devices such as cardiovascular stent, neuro thrombectomy retriever and aortic valve scaffold. Hydrogen at a concentration of  $C_H < 100$  wppm is almost always contained in these devices due to the chemical surface treatments during production. The survey of hydrogen concentrations in 9 commercial stent samples show H concentrations values ranging from 6 to 55 wppm. Correspondingly, hydrogen (8 wppm and 40 wppm) is charged to NiTi samples at two thermal-treatment states (500°C-annealed and 800°C-annealed) for comparative studies. The effects of hydrogen are revisited to clarify the hydrogen-induced changes of the operating deformation mechanism and the subsequent reduction of ductility in NiTi of both states. *In-situ* investigations at mesoscopic length scale (50-500  $\mu\text{m}$ ) are performed using electron backscatter diffraction (EBSD) mapping during tensile deformation of the 800°C-annealed samples. The deformation microstructure and the operating deformation mechanism are further studied at microscopic length scale ( $< 5 \mu\text{m}$ ) by transmission electron microscopy (TEM) for both 500°C and 800°C annealed samples. The results display that the influence of 8 wppm H on final material properties is insignificant in 500°C and 800°C annealed samples. However, for both, a concentration of 40 wppm H noticeably decreases the martensitic transformation temperature and the macroscopic

ductility of the samples. In the 800°C-annealed sample, *in-situ* EBSD observes that the propagation of martensite band (MB) has finished at  $\epsilon=0.1$  in the 8 wppm H sample while the propagation seems interrupted in the 40 wppm H sample until the same strain. Inside and surrounding the MB, island-like non-transformed austenite zones are formed representing 14.8area% of the observation zone. In both 500°C and 800°C annealed samples, TEM observations found extensive dislocation activity in specific regions of the samples after being charged to 40 wppm hydrogen. Thermal desorption spectroscopy (TDS) confirms that a hydrogen redistribution has happened in the 40 wppm hydrogen during the homogenization process. The change of local operating deformation mechanism from martensitic transformation to dislocation slip is thought to be responsible to the changes of mechanical properties of hydrogen-charged NiTi. The effect is further discussed in relation to the redistribution of hydrogen due to trapping at structural defects. In general, the results suggest that the influence of 8 wppm hydrogen is insignificant on the mechanical properties of NiTi, whereas the NiTi containing 40 wppm hydrogen may present risks of hydrogen-related mechanical failure within the strain amplitude range of a stent crimping process.

## 1. Introduction

For decades, nickel-titanium (NiTi) has been used in medical devices because of the large superelastic strain (about 7%) due to a reversible thermoelastic martensitic transformation [1,2]. This unique property is widely used in biomedical devices such as self-expandable cardiovascular stents. The deployment of a stent immediately after angioplasty has been shown to significantly decrease the risk of restenosis [3]. Currently, the majority of NiTi stents are of the self-expandable type. These devices, usually fabricated into a mesh tubular stent by laser process of a NiTi tube, are annealed at about 500°C into a diameter, which is higher than the targeted artery. The austenite finish ( $A_f$ ) temperature of the shaped stent is usually around 22°C, lower than body temperature (37°C) for superelastic self-expansion. The final NiTi stent needs to be crimped (radially deformed by compression) into a small diameter catheter for transportation in the cardiovascular system. Before crimping, the stent is fully austenitic (B2, CsCl-type crystal structure). After crimping, the effect of this deformation (the maximum local strain can reach  $\epsilon=0.06 - 0.1$ ) causes the transformation of the austenite into martensite (B19', monoclinic structure). After being located at the implantation site in

the artery, the NiTi device is pushed out of the catheter and immediately and automatically self-expands by the reversion from B19' (stress-induced martensite, SIM) to its parent B2 phase in order to conform to the walls of the artery vessel with a steady radial force [4]. Then, the stent can be subjected to cyclic pulsating loads due to heart beating (typically  $4 \cdot 10^7$  cycles/year).

To achieve this functionality (with the suitable subsequent radial force), the NiTi stents are required for partially recrystallized microstructure with a characteristic austenite finish ( $A_f$ ) temperature about 22°C inferior to body temperature (37°C) for stable superelastic recovery and a ductility up to about  $\epsilon=0.1$  in tensile/compression strain for being crimped safely into the catheter.

Conventional defects in stents have been intensively studied and strictly inspected in production, e.g. non-metallic inclusions [5] and surface defects [6], to ensure the long-term structural integrity and superelastic functionality of every single product. However, during the production stages, hydrogen absorption occurs frequently during acid washing and electropolishing processes [7]. This fact may be critical since it has been often reported that the contamination of hydrogen can lead to several detrimental effects such as: (1) suppression of martensitic phase transformation [8–12], (2) noticeable increase of the transformation stress threshold [7,8,10,11,13,14] and (3) embrittlement [7,10,13,15–18]. Recently, Duerig *et al.* [19] have pointed out several aspects of hydrogen in Ni-Ti and highlighted both localized and highly dynamic effects. It was shown that a content as low as 100 wppm hydrogen at fully homogenized distribution may completely suppress the austenite–martensite transformation. It was also reported that the ductility was drastically affected in a time-dependent manner based on the diffusion of hydrogen: the tensile samples are fully ductile after charging, but become fully brittle hours later.

In the industrial practice, at “high concentrations” ( $C_H > 100$  wppm), the hydrogen contaminated stents can possibly be ruled out during quality inspection by  $A_f$  temperature measurements or mechanical compression tests. In contrast, for “low hydrogen concentrations” ( $C_H < 100$  wppm), the hydrogen-containing stents may pass the quality inspection to be finally crimped into the catheter for implantation. According to the conclusion proposed recently by Duerig *et al.* [19], the safety limit of 50 wppm hydrogen in average, required by ASTM F2063 [20] standard for wrought NiTi material, was still considered to be sufficient for the finished NiTi material and devices under condition that the hydrogen was homogeneously distributed. The excessive hydrogen, generally or locally, may lead to

the formation of micro-cracks and to struts fracture during crimping. These structural defects can result in implantation failure due to the difficulty of releasing the stent from the catheter and the incomplete self-expansion. High-risk surgery is usually required to remove the failed stent, but sometimes leads to the severe adverse events to the patients whose conditions are not suitable for invasive operation.

The objectives of this study are to study the effects of hydrogen in austenitic NiTi exhibiting superelasticity for different hydrogen concentrations. The concentrations (8 and 40 wppm) are selected according to the actual hydrogen level in the current commercial NiTi stents. In order to study the H-charged samples by *in-situ* and *ex-situ* methods, two different starting microstructures (partially and fully recrystallized) are submitted to microstructural and mechanical investigations. Towards the understanding of mechanisms, the effects of hydrogen concentration and redistribution are revisited in the NiTi materials for the implication on NiTi stent safety with respect to the present acceptance of hydrogen concentration.

## **2. Materials and methods**

### ***2.1. Samples realization and specification***

For this study, samples are prepared by using commercial ELI grade (Extra Low Inclusion grade) NiTi plate (0.5 mm thickness) from Johnson Matthey®. The raw NiTi plate is received at as-rolled state. All the NiTi samples are cut from the same NiTi plate and annealed to obtain partially and fully recrystallized states under vacuum ( $2 \times 10^{-5}$  mbar). The partial recrystallization is conducted at 500°C for 6 minutes to obtain the same starting microstructure and austenite finishing temperature ( $A_f$ ) as commercial stents, hereafter called “500°C-annealed”. The full recrystallization is obtained after 10 minutes spent at 800°C (i) to desorb the hydrogen potentially in the raw NiTi plate and (ii) to obtain an equiaxial grain structure with average grain-size of 25  $\mu\text{m}$  for *in-situ* electron-backscattered diffraction (EBSD) studies. The fully recrystallized state will thereafter referred to as “800°C-annealed”. Both annealing treatments are finished by water quenching.

For hydrogen charging, two concentrations are selected for being representative of the commercial products on the market (low range and high range). To evaluate the H compositional range into these products, a complete thermal desorption spectroscopy (TDS) investigation has been conducted on

nine different self-expandable NiTi peripheral stents from eight different trademarks (kept anonymous in the frame of this paper). These stent products have been stored at room temperatures for several months since the date of production. The observed results display a hydrogen concentration range spreading out from 6 to 55 wppm (Table 1). It can be noticed that 8 of the 9 stents exhibit hydrogen concentrations below the 50 wppm ASTM F2063 standard acceptance; only one is slightly over. The TDS spectra obtained from the stent samples are similar in form. The spectrum of Stent 4 analyzed by Gaussian peak deconvolution is shown in Section 3.4 to show the hydrogen distribution.

*Table 1: The hydrogen concentrations of current commercial stents in Europe.*

Product	Stent 1	Stent 2	Stent 3	Stent 4	Stent 5	Stent 6	Stent 7	Stent 8	Stent 9
H (wppm)	15± 1.5	20± 2.0	14± 1.0	33± 3.0	35± 3.5	19± 2.0	7± 0.5	55± 5.5	6± 0.5

From this set of values, two different hydrogen concentrations, 8 wppm (representative of the low concentrations range) and 40 wppm (representative of the high concentrations range) were selected and used as target for the present study.

The hydrogen-containing samples are prepared by immersion in the modified Kroll's reagent (HF: HNO<sub>3</sub> = 1:3) at 60°C for different durations to obtain the target concentrations. In order to quantify the hydrogen concentration, 5 mm length specimens are cut from each sample. The hydrogen charged samples are aged at room temperature (RT) for 192 hours before experiments. For comparison, a 40 wppm H sample is also analyzed by TDS after only 24 hours RT aging to verify the hydrogen redistribution.

## **2.2. Characterization methods**

The hydrogen concentrations of the NiTi samples are accurately quantified by using the melting extraction technique on a Bruker™ Galileo G8 apparatus. The stent samples and some of the NiTi samples are analyzed by thermal desorption spectrometry (TDS) under an initial vacuum of 5.10<sup>-7</sup> mbar, by heating up to 1000°C at a heating-rate of 10°C/min. Differential scanning calorimetry (DSC) measurements (Mettler Toledo DSC3 from 80°C to -120°C at 5°C/min under controlled atmosphere)

are performed to identify the phase transformation temperatures.

Uniaxial tensile tests (single loading to fracture tests and cyclic loading-unloading tests) are performed at a constant strain rate of  $2 \cdot 10^{-3} \text{ s}^{-1}$  using an Instron 5966 apparatus with a 10 mm extensometer, at  $A_f + 15^\circ\text{C}$  temperature. The tensile samples are in the same dimensions at gauge length (L20mm x W4mm – 0.5mm thickness). The macroscopic tensile deformation in the plateau range proceeds in a localized manner in both  $500^\circ\text{C}$  and  $800^\circ\text{C}$  annealed samples, that stress-induced martensite (SIM) takes place locally then propagates along the tensile axis.

A scanning electron microscope (Zeiss Leo 1530 FEG-SEM operated at 20kV) is used to perform observations by secondary electron imaging (SEI) and EBSD. An in-SEM tensile device (Micromecha Proxima 100) is used to apply in-situ tensile strain on the specimens for SEI and EBSD observations until fracture at ambient temperature. The *in-situ* samples are in the shape of long straight plates in the dimensions of L40mm x W2mm – 0.5mm thickness. The gauge part at the center of the in-situ sample is slightly polished to have a geometry of L10mm x W2mm – 0.45mm thickness to improve the EBSD quality and to concentrate the deformation for observation. The surface polishing is processed at room temperature on the in-situ samples after 192 hours aging. The polishing process has been verified by hydrogen quantifications before and after polishing process on NiTi samples at different annealed states. No increasing of hydrogen concentration has been detected. The sample surface and the propagation of macroscopic Lüders-band like martensite band front (MBF) are monitored during the *in-situ* traction process by SEI. Five EBSD mappings are repeated at the same zone during each in-situ test at different strain states. The number of scans is limited by the progressive surface contamination from each scan. The SEI and EBSD mapping are conducted under stress by holding the tensile strains.

A transmission electron microscope (JEOL 2100plus operated at 200 kV) is used to observe the post-mortem specimens after specific tensile straining. Struers Tenupol-5 (methanol +  $\text{HClO}_4$  at  $-10^\circ\text{C}$ ) is used to prepare the TEM thin foils.

### **3. Results**

#### **3.1. DSC measurements and tensile tests**

The martensitic transformation process is characterized by DSC measurements on the two 500°C-annealed (partially recrystallized) samples (8 and 40 wppm H) prior to deformation. The corresponding DSC curves are shown in Figure 1a.

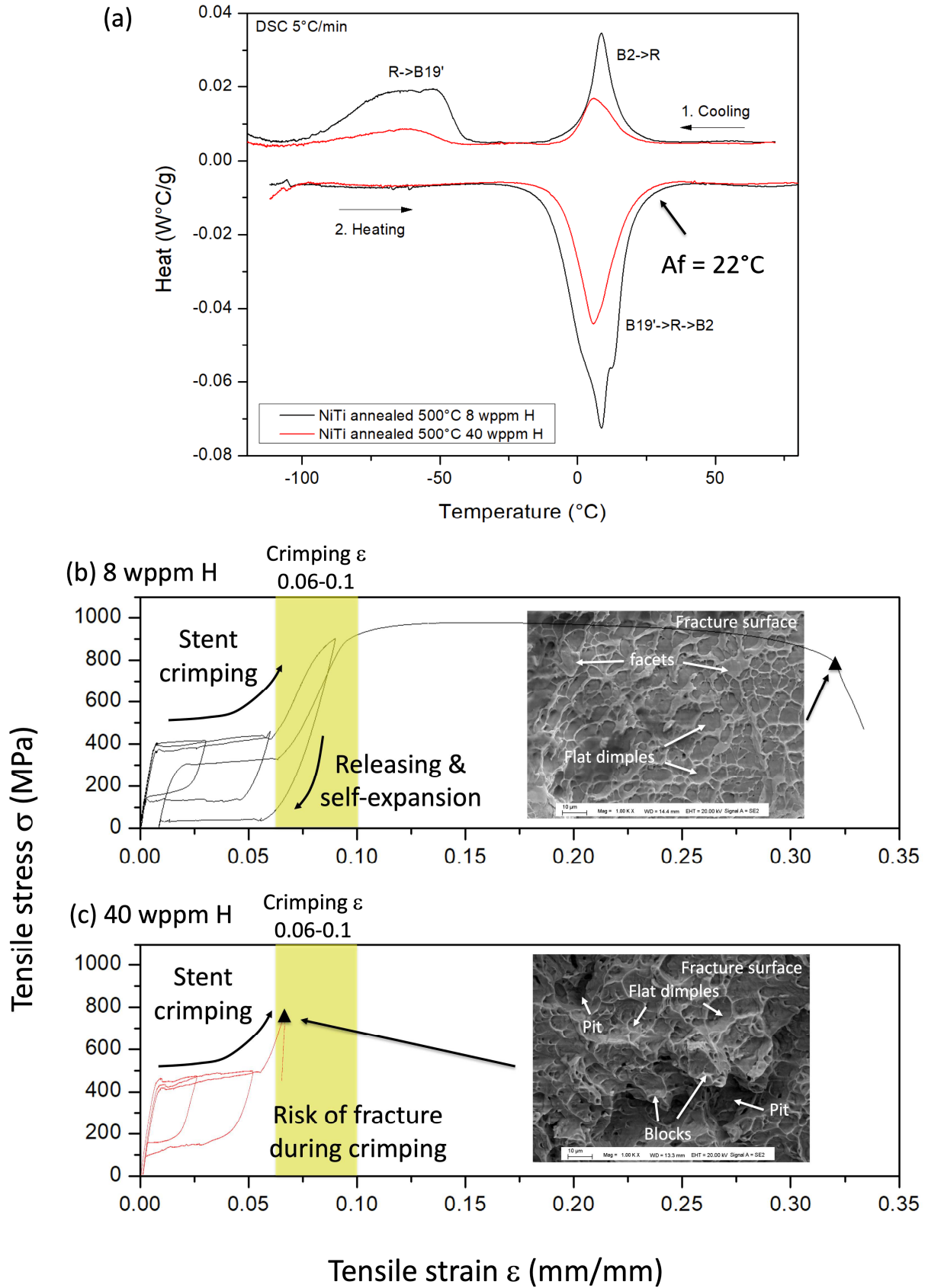


Figure 1. Thermal and mechanical characterizations of 500°C-annealed NiTi after hydrogen-charging. (a) DSC curves of 8 wppm H sample (black) and 40 wppm H sample (red), a two-step martensitic

transformation (B2-R-B19') is observed in each sample; (b) Uniaxial cyclic loading-unloading tensile test on the 8 wppm H sample (black) at  $A_f+15^\circ\text{C}$ : three unloading cycles are performed at  $\epsilon=0.03, 0.06, 0.09$  then the sample is reloaded until fracture (deformation rate =  $10^{-3} \text{ s}^{-1}$ ); (c) Cyclic loading-unloading of 40 wppm H sample under the same testing conditions. The maximum strain amplitude ( $\epsilon=0.06-0.1$ ) corresponding to stent crimping and self-expansion is marked in yellow range in figure (b) and (c). The micrographs of the fracture surfaces are shown as insets in figure (b) and (c) for each sample after fracture, respectively. The fracture points on the tensile curves are marked by the black triangles.

The phase transformations and transformation temperatures are summarized in Table 2. Both of the  $500^\circ\text{C}$ -annealed samples exhibit two-step martensitic transformation (B2-R-B19'). The R-phase, trigonal structure, is presented as a competing martensite phase to B19'. In the  $500^\circ\text{C}$ -annealed NiTi from as-rolled state, the high density of rearranged dislocations and precipitates present in the structure (shown in section 3.3) tend to suppress B19' transformation with respect with R-phase transformation [21]. In presence of hydrogen, the transformation peaks of both transformations reduce in area when the hydrogen concentration raises from 8 wppm to 40 wppm. Moreover, the  $M_s$  (R-B19') temperature shows a slight shift towards lower temperatures when hydrogen increases to 40 wppm. Meanwhile, the  $A_f$  temperature ( $22^\circ\text{C}$ ) does not seem to be affected for the two samples. The phenomena underline a suppression effect of hydrogen on both transformations, but the B19' transformation seems more sensitive to the hydrogen concentration than the R-phase transformation.

Table 2: Results of DSC measurements for each microstructure and H content.

Sample	Hydrogen concentration (wppm)	Transformation sequence	$M_s$ (B19')	$A_f$
500°C-annealed	$8 \pm 2$	B2-R-B19'	$-40^\circ\text{C}$	$\approx 22^\circ\text{C}$
	$40 \pm 5$	B2-R-B19'	$-47^\circ\text{C}$	$\approx 22^\circ\text{C}$
800°C-annealed	Before H charge	B2-B19'	$-15^\circ\text{C}$	$\approx 4^\circ\text{C}$
	$8 \pm 4$	B2-B19'	$-15^\circ\text{C}$	$\approx 4^\circ\text{C}$

Figures 1b and 1c display the cyclic tensile curves of the two hydrogenated 500°C-annealed samples. Perfect superelastic recoveries are achieved by both samples up to  $\epsilon=0.06$ , which is the range for stent service in the artery. However, a drastic ductility loss for the 40 wppm H sample (fracture at about 0.07) is noticed when comparing to the 8 wppm H one (fracture at over 0.3). When comparing the results to the maximum crimping strain ( $\epsilon=0.06-0.1$ , marked in yellow in Fig. 1b and 1c), a risk of fracture can be a concern for the 40 wppm H sample. The micrographs of fracture surface are shown as insets near the two tensile curves. Features of flat dimples and facets can be seen on the 8 wppm H sample, whereas morphologies like blocks and pits can be noticed in addition to the flat dimples on the 40 wppm H sample. The blocks and pits are of about 10  $\mu\text{m}$  diameter in sizes. The change of the fracture surface may result from a change in deformation mechanisms.

In the 800°C-annealed samples, the martensitic transformation process in the fully recrystallized starting microstructure is characterized by DSC measurements on the three samples (as-800°C-annealed, 8 and 40 wppm H) prior to deformation. The corresponding DSC curves are shown in Figure 2a.

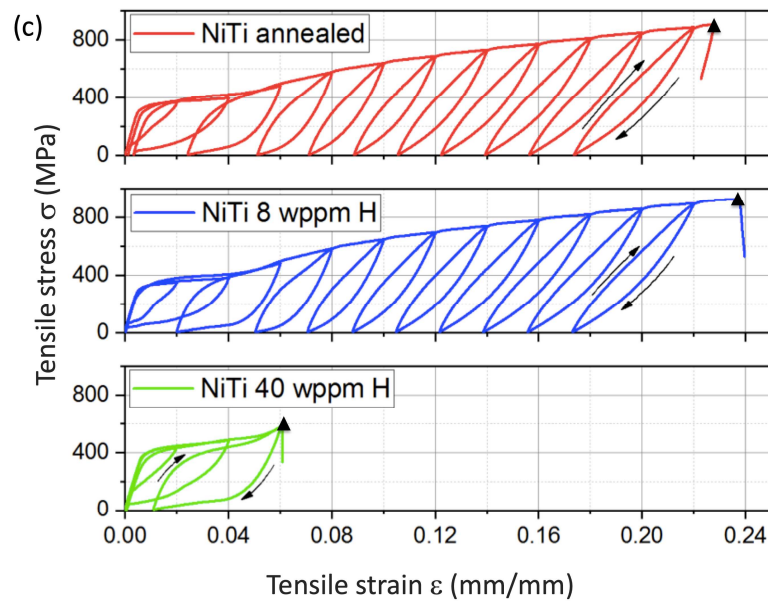
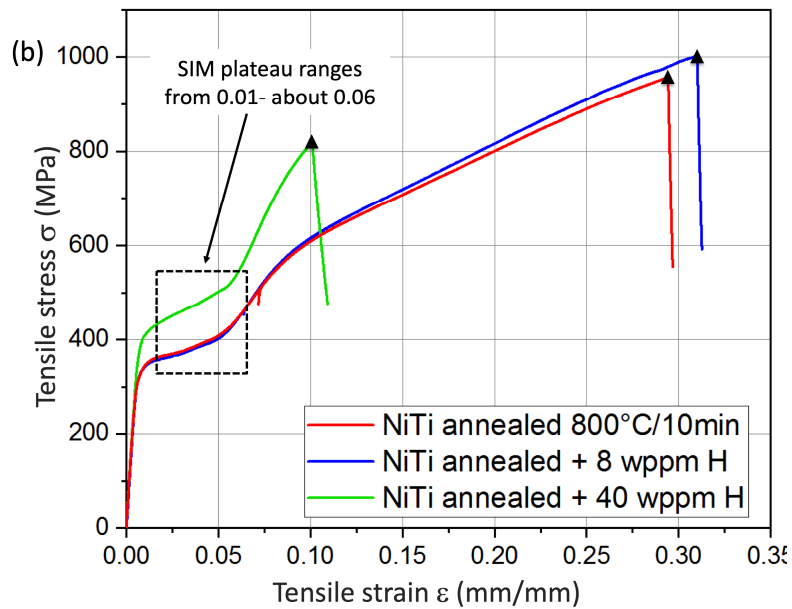
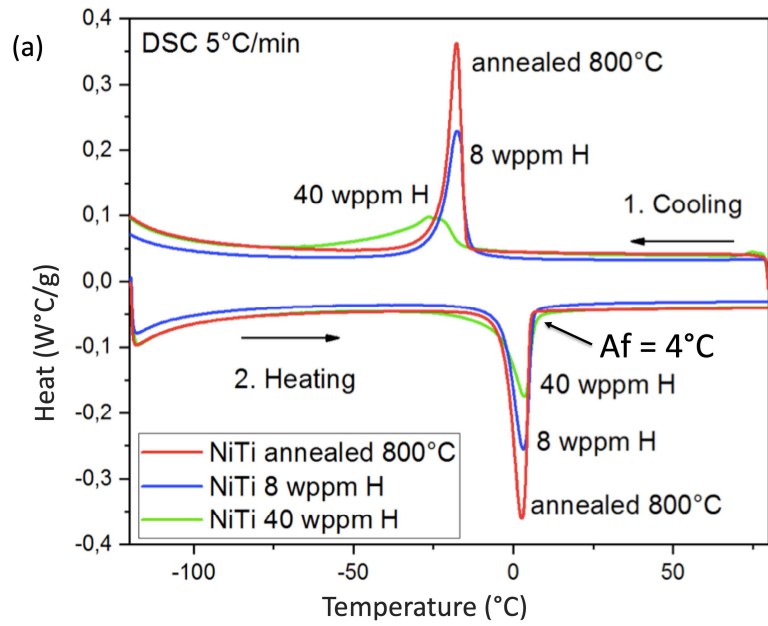


Figure 2. Thermal and mechanical characterizations of 800 ° C-annealed NiTi after hydrogen-charging. (a) DSC curves of as-800°C-annealed sample (red), 8 wppm H sample (blue) and 40 wppm H sample (green) following the cooling-heating passage at 5°C/min, a single step martensitic transformation (B2-B19') is observed in each sample; (b) Curves of uniaxial single loading-to-fracture tensile test of the as-800 ° C-annealed sample (red), 8 wppm H sample (blue) and 40 wppm H sample (green) at Af+15°C; (c) Curves of uniaxial cyclic loading-unloading tensile test of the three samples under the same conditions; the unloading cycles are performed at  $\epsilon=0.02, 0.04, 0.06, 0.08\dots$  until fracture. The deformation rate is  $10^{-3} \text{ s}^{-1}$  in both single loading and cyclic loading-unloading tests. The fracture points on the tensile curves are marked by the black triangles.

The DSC results are summarized in Table 2. The martensitic transformation is the classic one-step process after full recrystallization between austenite (A) and martensite (M) [18]. The three samples are fully austenitic at RT (22°C), the stress-induced martensitic (SIM) transformation is triggered by tensile stress.

The single-loading curves of NiTi samples are shown in Fig. 2b, exhibiting typical “double-yielding” curves with a plateau in the elastic regime due to stress-induced martensitic transformation [21, 22]. The annealed and 8 wppm H samples exhibit almost identical characteristics regarding the stress-strain curves. The 40 wppm H sample exhibits a higher SIM plateau at about 420 MPa, (+23.5%) than the other two samples and a significant loss of ductility (fracture at  $\epsilon=0.1$ ).

Consistently with single-loading tests, the cyclic-loading results show similar behaviors for the 800°C-annealed and 8 wppm H samples and drastic ductility reduction in the 40 wppm H sample (Fig. 2c and Table 2). When comparing the behaviors between 500°C-annealed and 800°C-annealed samples, it can be noticed that the superelastic behavior of NiTi can be very dependent on microstructure and temperature [23].

### **3.2. In-situ EBSD characterizations on the 800°C-annealed samples**

In order to further investigate the hydrogen influence on the reversible martensitic transformation, *in-situ* SEM/EBSD observations under tensile strain are performed to compare the microstructural evolutions during tensile loading. The 800°C-annealed samples allow using EBSD to clarify the

fundamentals about the hydrogen influences to the martensitic phase transformation in B2 grains without perturbations of dislocation or nanoprecipitates. However, the EBSD technique is limited on the 500°C-annealed sample due to the sub-micrometric subgrain structure and high density of dislocations and nanoprecipitates (studied by TEM in Section 3.3). The Force-Elongation curves recorded during the in-SEM traction (Fig. 3a and 4a) exhibit the same shape and ductility as observed in the tensile tests (Fig. 1 and 2). The image of martensite band front (MBF) is captured in Fig. 3b, when it is propagating over the observation surface at  $\epsilon=0.035$ . The angle between MBF and loading axis is close to  $55^\circ$ , consistent with previous studies [24]. Fig. 3c shows a series of micrographs of the surface relief changes at  $\epsilon=0.06$ , 0.1 and 0.25 after the MBF has passed over the observation surface. The fresh fracture surface of the 8 wppm H sample shows dimple-like morphologies, a few micrometers in diameter, flat and uniformly distributed (Fig. 3d). The homogeneous dimple-like features suggest a ductile-type fracture of the material, in agreement with its good ductility. Similar to the “macroscopic” tensile test results (Fig. 2b), the elongation to fracture of the 40 wppm H sample as observed *in-situ* in the SEM set-up is also drastically reduced to  $\epsilon=0.1$  (Fig. 4a). No clear MB can be seen activated near the observation zone (shown in Fig. 4b) at the very beginning of the deformation ( $\epsilon=0.015$ ). Three SEI micrographs in Fig. 4c at  $\epsilon=0.06$ , 0.08 and 0.1 present the surface relief change during the in-SEM loading at the same observation zone as shown in Fig. 4b. Fig. 4d presents the fresh fracture surface exhibiting brittleness features, such as ridges and facets. The size and distribution of the dimples are non-uniform and in agreement with previous studies of the fractographies observed after hydrogen charging [9,12,18]. The fracture surface change, between 8 wppm H and 40 wppm H, may again suggest a change of deformation mechanisms in the 800°C-annealed samples, depending on the hydrogen amount.

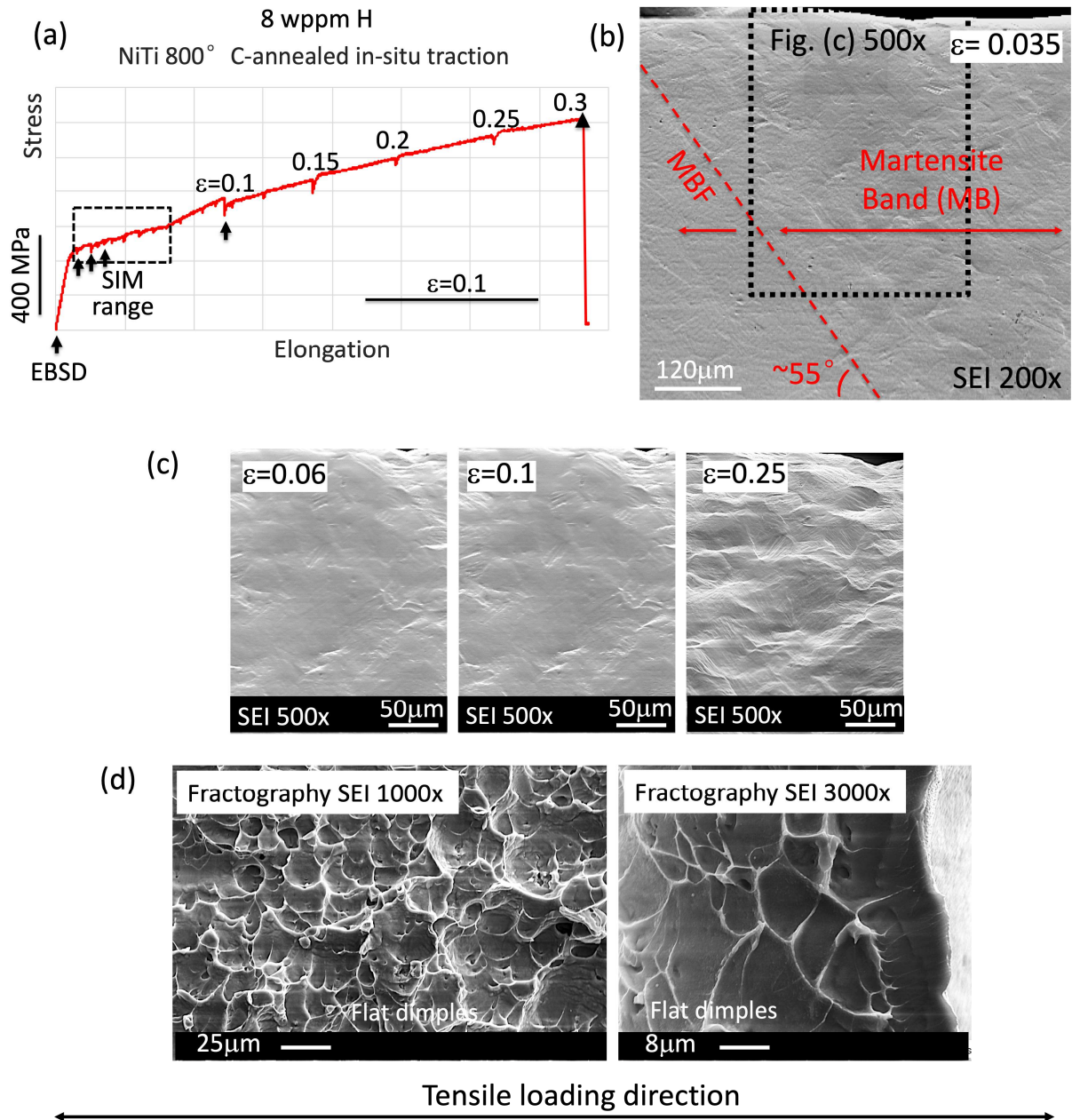


Figure 3: Force-elongation curve and micrographs of 8 wppm H sample (800°C-annealed) during in-situ traction in SEM. (a) Sample schema and in-situ force-elongation curve of the 8 wppm H sample; (b) Secondary electron imaging (SEI) micrograph (200x) of the martensite band front (MBF) crossing the observation area at  $\epsilon = 0.035$ . The MBF line is marked by red dash line, the propagation direction of the MBF is marked by red arrow, the angle between MBF line and loading axis is about  $55^\circ$ ; (c) A series of SEI micrographs (500x) at the same observation area captured at  $\epsilon = 0.06, 0.1, 0.25$ ; (d) The SEI micrographs of the fresh fracture surface, on which shallow dimples are observed. The fracture points on the tensile curve are marked by the black triangle. The holding points for EBSD mapping are marked by vertical arrows.

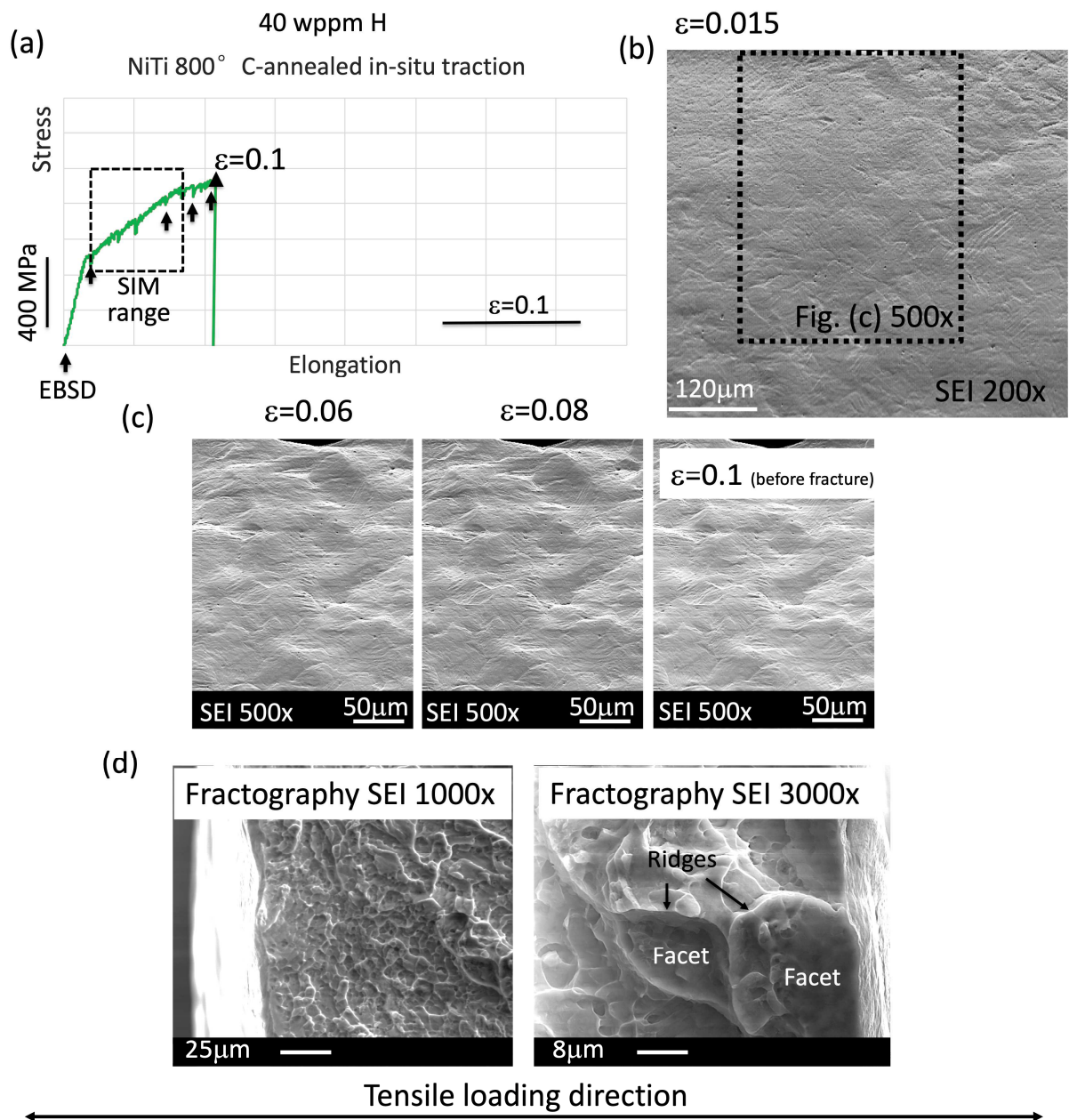


Figure 4: Force-elongation curve and micrographs of 40 wppm H sample (800°C-annealed) during in-situ traction in SEM. (a) Sample schema and in-situ force-elongation curve of the 40 wppm H sample; (b) Secondary electron imaging (SEI) micrograph (200x) of the observation area, no clear martensite band front (MBF) can be seen; (c) A series of SEI micrographs (500x) at the same observation area are captured at  $\epsilon = 0.06$ ,  $0.08$ ,  $0.1$  before fracture; (d) The SEI micrographs of the fresh fracture surface, on which flat dimples in mixture with ridges and facets are observed. The fracture points on the tensile curve are marked by the black triangle. The holding points for EBSD

*mapping are marked by vertical arrows.*

*In-situ* EBSD mapping is performed in the  $\epsilon=0-0.1$  range to monitor the overall surface fraction of martensite as a function of tensile strain, and to trace the local deformation mechanism on loading. Before tensile loading, the 8 wppm H sample presents a fully recrystallized microstructure of B2 austenite (Fig. 5a). As shown by IQ+phase EBSD maps, in Fig.5b, plate-like B19' martensite is stress-induced upon loading in the B2 parent grains along with the MBF propagation. The SIM growth is featured by progressive multiplication and thickening of martensite plates (Fig. 5b). It should be noticed that the propagation of the martensite band seems reluctant when comparing to the classic propagation manner, in which the martensitic transformation stops after the MBF passes over. The phenomenon could probably relate to the reduced gauge size of *in-situ* tensile samples. Or another hypothesis is that the hydrogen could promote the localization of deformation in MBs but suppress the macroscopic deformation localization. At  $\epsilon=0.1$ , the EBSD mapping (Fig. 5c) confirms that most of the B2 grains have transformed to martensite. The surface fraction of the non-transformed B2 phase is about 3.2%. Attention is paid to the formation of  $\{114\}_{B2}$  type B2 twinning from  $\{201\}_{B19'}$  type deformation twin precursor as accommodation mechanism to the increasing local strain [25-27]. However, the  $\{114\}_{B2}$  twin is not observed during the *in-situ* loading process, neither in 8 wppm H nor in 40 wppm H 800°C-annealed samples.

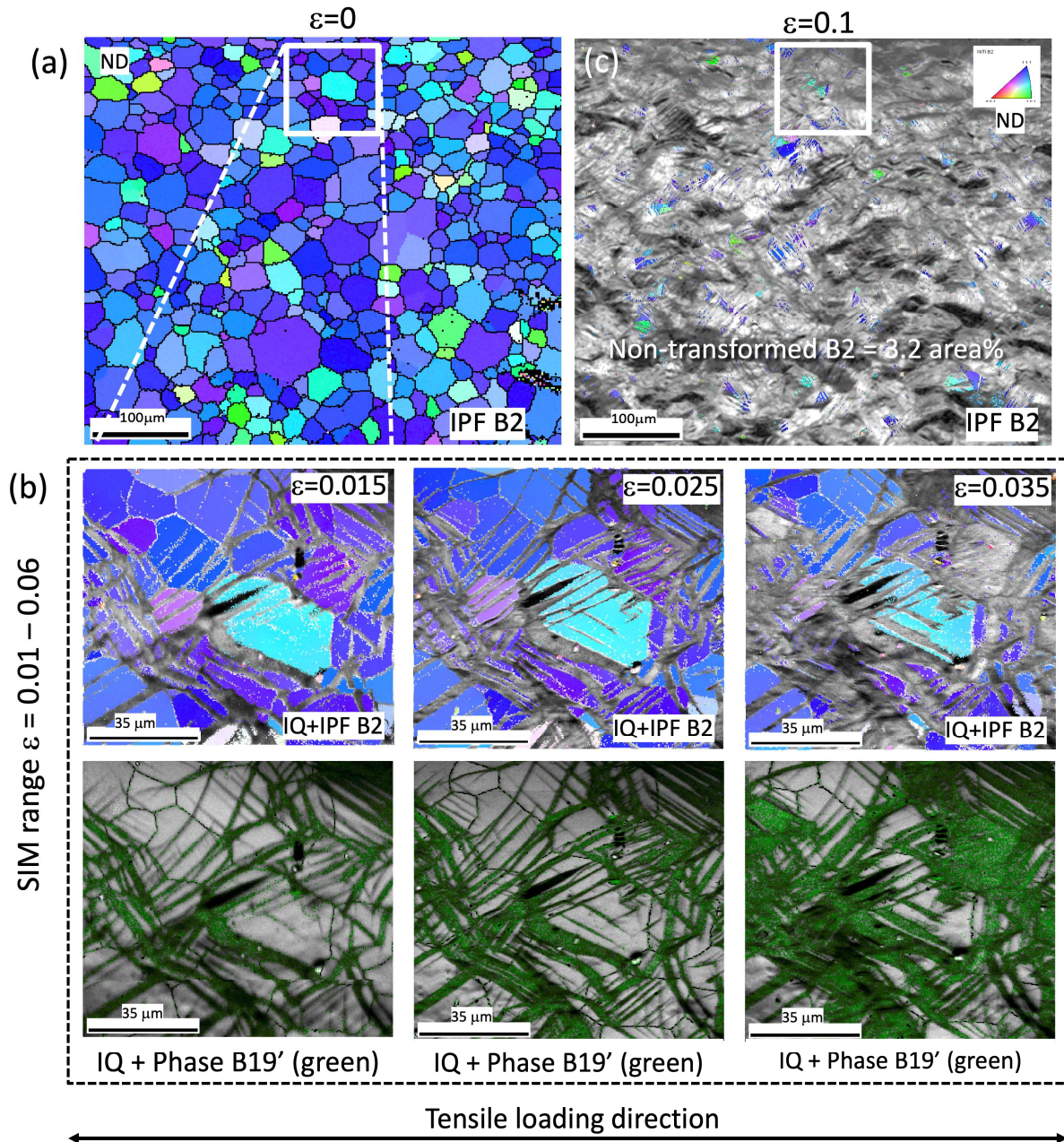


Figure 5: EBSD maps of 8 wppm H sample ( $800^{\circ}\text{C}$ -annealed) recorded during in-situ traction process. The EBSD scans are performed by holding the deformation strains without unloading. The deformation microstructures are traced by five EBSD scans at  $\epsilon = 0, 0.015, 0.025, 0.035$  and  $0.1$ , respectively. (a) Inversed pole figure (IPF) map of B2 phase before deformation at the 500x zone shown in figure 3b; (b) IPF+IQ maps of B2 phase and the corresponding phase maps of B19' martensite at  $\epsilon = 0.015, 0.025, 0.035$  at 1000x magnification at the zone marked by white square in (a). The micrographs show the progressive growth of B19' martensites in B2 grains when martensite band front (MBF) propagates across the observation zone (the same 200x zone shown in figure 3b); (c) the IPF+IQ map of B2 phase at  $\epsilon = 0.1$  at the same observation zone (500x). The area fraction of

*non-transformed B2 phase is 3.2%. The 1000x zone is marked by white square, in which some non-transformed B2 phase can still be seen, but in lower area fraction when comparing to (b).*

*In-situ* EBSD characterizations are similarly performed on the 40 wppm H samples (see micrographs in Figure 6). The initial microstructure appears to be similar to the 8 wppm H sample (Fig. 6a), i.e. fully austenitic and recrystallized. First SIM plates form around  $\epsilon=0.015$  at the observation zone (Fig. 4b and 6b). When comparing to 8 wppm H sample, clear differences in microstructural evolutions start to be obvious when  $\epsilon$  reaches 0.06. At mesoscopic scale, the stress-induced transformation seems concentrated in band-like area, forming a MB (shown in Fig. 6c). Inside and surrounding the MB, the martensitic transformation is inhibited in many B2 regions, like “islands” (Fig. 6b). One of the islands is observed about its formation (marked by the yellow dashed line in Fig. 6b), during which martensite plates are reluctant to grow towards the core of the island. The core is a triple-junction of three neighboring grains. In the view of a larger area (Fig. 4c), the total area fraction of the non-transformed B2 “islands” is 14.8% before the sample breaks in the test ( $\epsilon=0.1$ ).

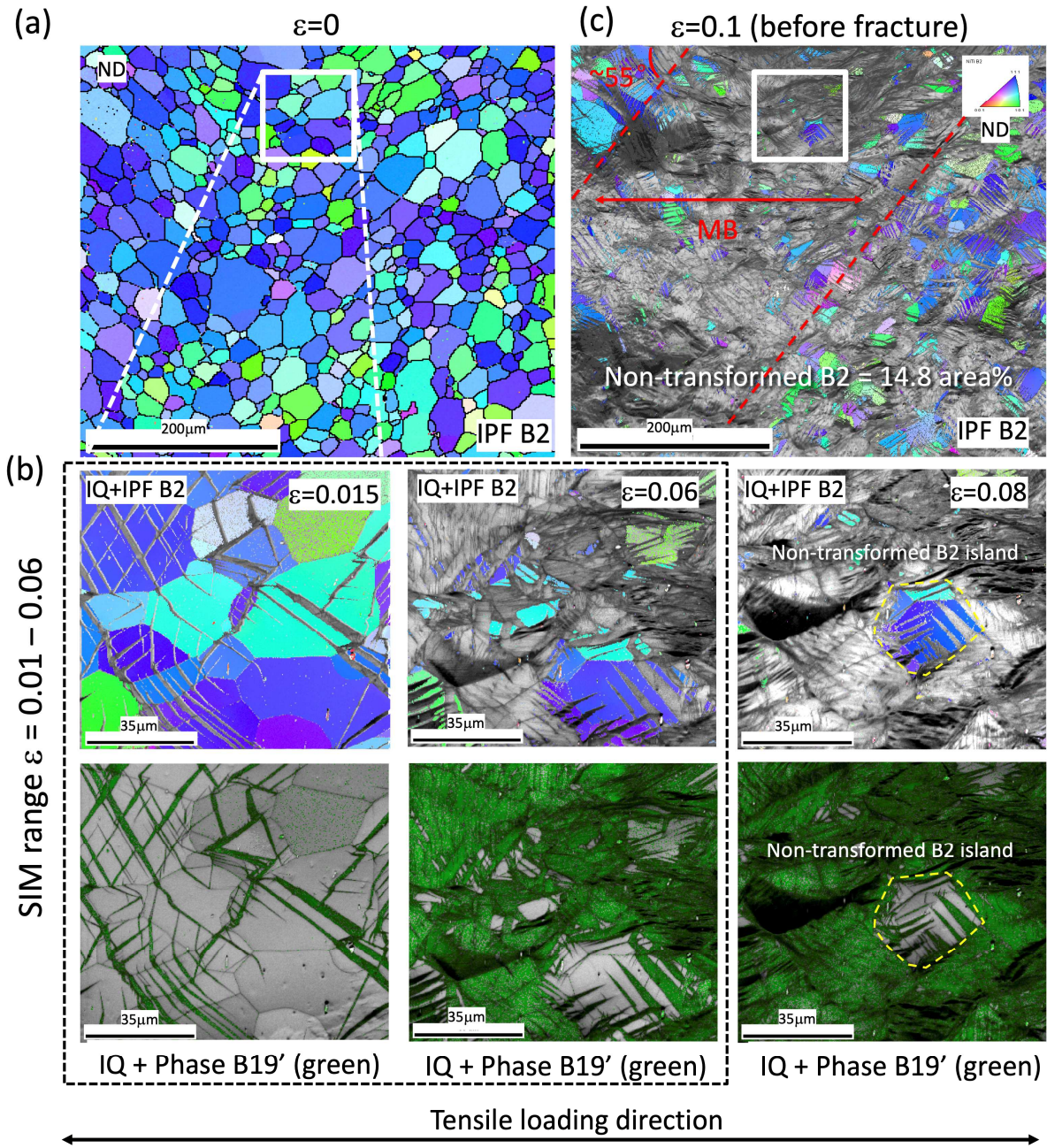
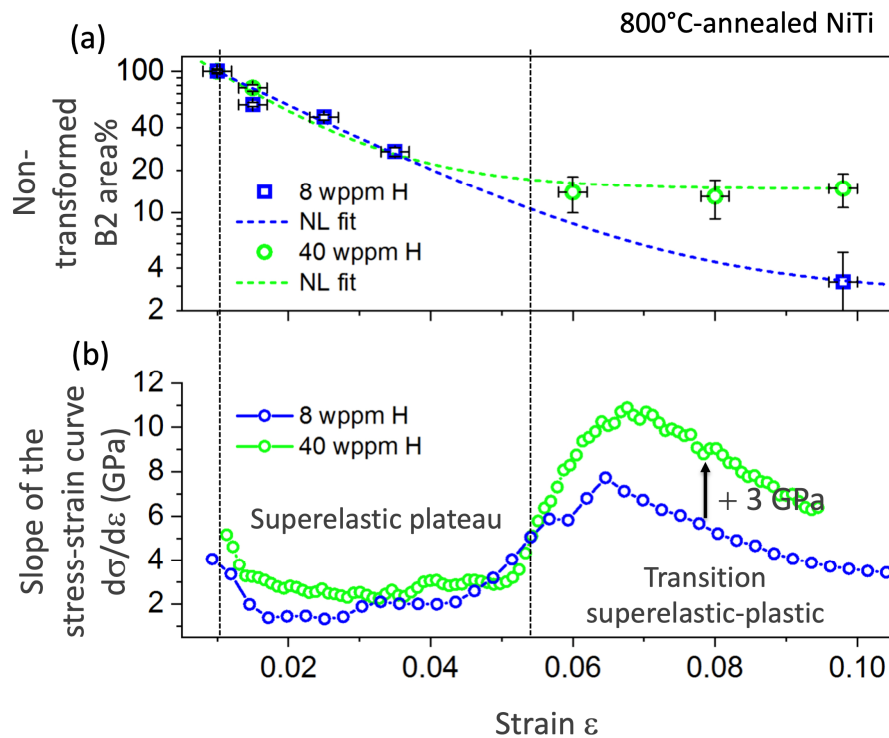


Figure 6: EBSD maps of 40 wppm H sample (800°C-annealed) recorded during in-situ traction process. The EBSD scans are performed by holding the deformation strains without unloading. The deformation microstructures are traced by five EBSD scans at  $\epsilon = 0, 0.015, 0.06, 0.08$  and  $0.1$  before fracture, respectively. (a) Inversed pole figure (IPF) map of B2 phase before deformation at the 500x zone shown in figure 5b; (b) IPF+IQ maps of B2 phase and the corresponding phase maps of B19' martensite at  $\epsilon = 0.015, 0.06, 0.08$  at 1000x magnification at the zone marked by white square in (a). The micrographs show the progressive formation of a non-transformed B2 island (marked by yellow dash line); (c) the IPF+IQ map of B2 phase at  $\epsilon = 0.1$  at the same observation zone (500x). A MB can

be observed, denoted by red dash lines and arrows. The area fraction of non-transformed B2 phase is 14.8%. The white square shows the 1000x zone observed in (b).

To summarize observation made on the 800°C-annealed samples, the area fractions of non-transformed B2 phase versus tensile strain (Fig. 7a) can be compared between the two H-charged samples. The minimum fraction of non-transformed B2 phase is achieved at  $\epsilon_t=0.05-0.06$  in the 40 wppm H sample which is earlier than 8 wppm H sample (after  $\epsilon_t=0.08$ ) (Fig. 7a). The slope of the stress-strain curve ( $d\sigma/d\epsilon$ ) is plotted in range  $\epsilon_t=0.01-0.1$ , including the SIM plateau and the superelastic-plastic transition (Fig. 7b). It can be seen that the two slopes are almost identical before the minimum fraction of non-transformed B2 phase is reached in 40 wppm H sample. Afterwards, the slope of the 40 wppm H sample increases rapidly to 3 GPa higher than that of 8 wppm H sample. The 3 GPa difference is kept until tensile fracture of the 40 wppm H sample. This difference could be related to the change of deformation mechanism between the two samples. At  $\epsilon=0.1$  (under loading before fracture), it can be observed from EBSD (Fig. 3c and Fig. 4c) that 40 wppm H sample presented a high fraction (14.8 area%) of B2 islands whereas the microstructure of the 8 wppm H sample is composed by much less non-transformed B2 phase (3.2 area%).



*Figure 7: Plotting of the non-transformed B2 area fractions and the slope of the stress-strain curve as a function of tensile deformation strain of the 800°C-annealed samples. (a) Plots of the area fractions of non-transformed B2 phase of 8 wppm H sample (blue open square) and 40 wppm H sample (green open square) obtained from in-situ EBSD measurements. Non-linear fitting curves of every samples are shown in dash lines, respectively using the same color; (b) The slope of the stress-strain curve obtained from single tensile loading curves are plotted in dot-lines for 8 wppm H sample (blue) and 40 wppm H sample (green).*

### **3.3. TEM observations on the 800°C and 500°C annealed samples**

In order to investigate the operating deformation mechanism and the non-transformed B2 islands, TEM observations are performed on the 800°C-annealed, hydrogen-charged, samples after tensile deformation to  $\epsilon=0.1$  (Fig. 8).



and  $b_3$  are materialized by yellow dashed lines. (d) A B19' martensite plate and selection area (SA) diffraction pattern (see inset); (e) Dark-field (DF) image of the B19' plate; (f) BF image of the B2 phase next to the B19' plate (see SA diffraction pattern in inset); (g) Orientation relationship (OR) between the B19' plate (poles in red open cycles) and the nearby B2 phase (poles in black dots) by stereographic projection. The common poles are marked by black dashed squares.

At  $\epsilon=0.1$ , as shown in Fig. 8a, a number of residual martensite plates are observed under bright-field contrast, showing two principal variants (noted as B19' V1 and B19' V2). The TEM foil is tilted to  $[111]_{B2}$  zone axis for dislocation imaging and B19' analysis. Fig. 8b and 8c present dislocation contrasts in the B2 matrix. Two-beam conditions are established to characterize each of the three dislocation types using  $g=[01-1]_{B2}$  (Fig. 8b) and  $g=[0-11]_{B2}$  (Fig. 8c) vectors. The g-vectors are marked by black arrows in Fig. 8b and 8c, respectively. Fig. 8b illustrates the contrasts of dislocations with two Burgers vectors  $b_1=a[001]$  and  $b_3=a[010]$  ( $a$  being the lattice parameter of B2), while  $b_2=a[100]$  is invisible due to the extinction condition  $g \cdot b=0$ . Fig. 8c displays the dislocation line contrasts of  $b_2=a[100]$  and  $b_3=a[010]$ , while  $b_1=a[001]$  extincts. The axis of the Burgers vectors  $b_1$ ,  $b_2$  and  $b_3$  are drawn in yellow dashed lines in the figures. Among the dislocations observed,  $b_3$  is particular in geometry, i.e. close to perfect straight lines: this feature has been reported as a signature of the dislocations formed during the reversion of B19' to B2 [28]. Such dislocation lines are left after the removing of the martensite interface during the shrinkage of the B19' phase. The lines are parallel to the traces of the internal twin boundaries of the vanishing B19' phase. It should be recalled that the TEM observations are made on the deformed samples after unloading. The stress relaxation results in the reversion of B19' to B2, which is partial in the 800°C-annealed samples.

The orientation relationship (OR) between the B19' and B2 matrix is analyzed at a martensite plate shown in Fig. 8d. The plate is tilted to  $[110]_{B19'}$  zone axis. The diffraction pattern of the selected area (SA) is shown in the inset of Fig. 8d. Bright-field image is captured by using the  $[1-10]_{B19'}$  reflection, shown in Fig. 8e. In order to determine the OR with respect to the B2 matrix, the TEM foil is tilted about  $6^\circ$  along A1 axis (shown in Fig. 8e) to the  $[111]_{B2}$  zone axis. The bright-field image along  $[111]_{B2}$  is shown in Fig. 8f with the SA diffraction pattern in the inset. Since the two zone-axes are

not exactly parallel, the corresponding stereo projection (Fig. 8g) is made to reconstruct the OR. The determined OR is close to  $(10\text{-}1)B19' // (21\text{-}1)B2$  and  $(010)B19' // (011)B2$ , consistent with the classic ones [21].

In the 40 wppm H 800°C-annealed sample, a non-transformed B2 island is found in the TEM foil (Fig. 9a), marked by yellow dashed line. When compared to the 8 wppm H samples, much higher density of  $\langle 001 \rangle$  screw dislocations can be observed with considerably reduced inter-spacing between adjacent dislocations. Three different Burgers vectors, noted as  $b_1=a[001]$ ,  $b_2=a[100]$  and  $b_3=a[010]$  in Fig. 9, are identified. Among them, the  $b_1$  dislocations are in much higher quantity than  $b_2$  and  $b_3$ , respectively. Owing to the local high dislocation density, it suggests that the SIM mechanism may not be the dominant deformation mechanism operating in the non-transformed B2 island. It has been reported that the hybrid slip/transformation activity in NiTi undergoing cyclic deformation [29], results in high density of dislocations due to repeating transformations between B19' and B2. However, the current sample is not cyclically deformed. The activation of dislocation slip could probably relate to the presence of hydrogen.

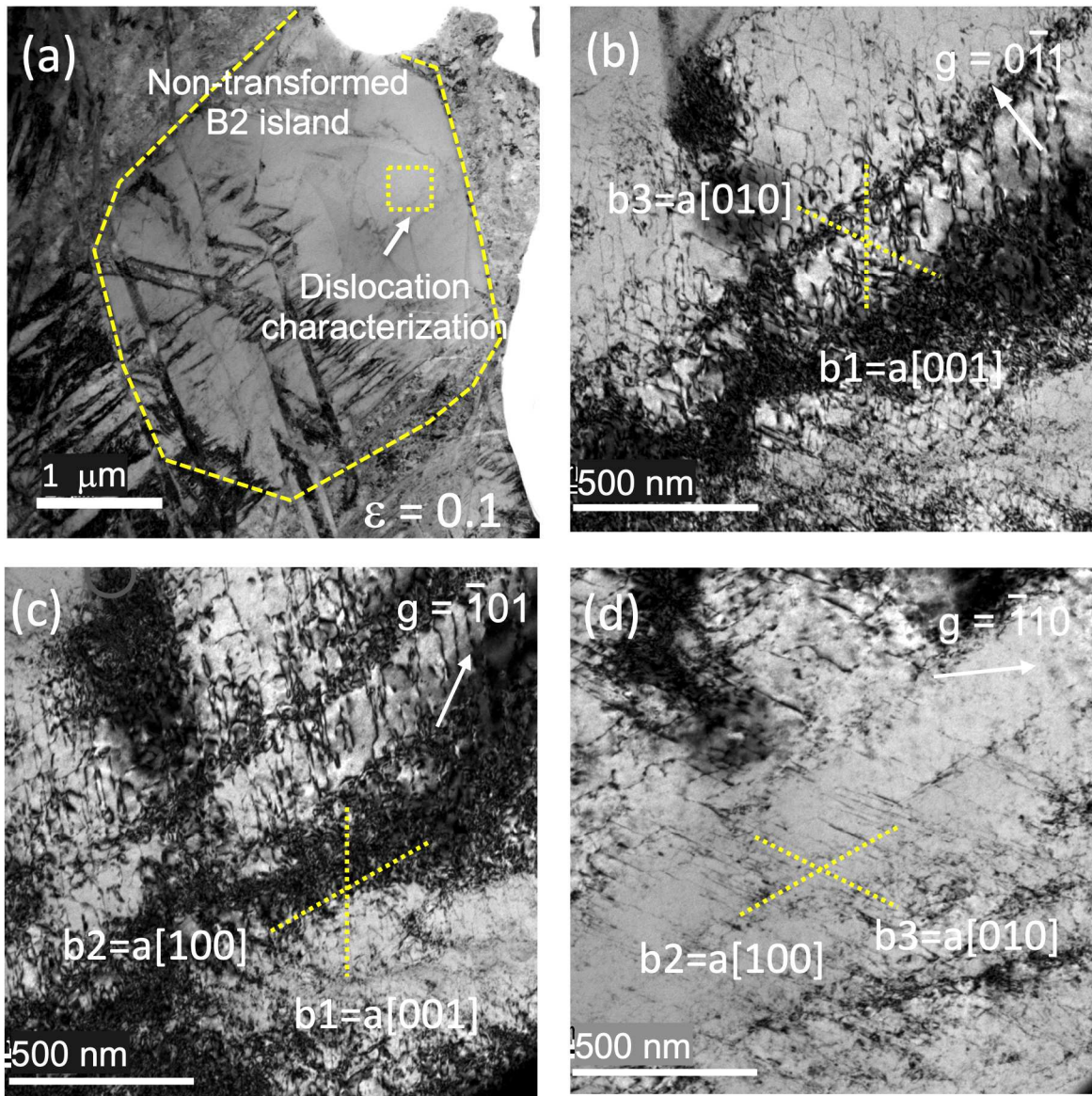


Figure 9: Micrographs of the TEM observation on the deformation microstructure of 40 wppm H sample (800°C-annealed). The TEM foil is prepared from the sample after single tensile loading to  $\epsilon=0.1$ . (a) Bright-field (BF) image of the deformation microstructure (out of zone axis), where a non-transformed B2 island can be seen (marked by yellow dash line). Dislocation characterization is performed at the squared area in the non-transformed B2 island; (b), (c) and (d) dislocation contrast imaging of  $b_1$ ,  $b_2$  and  $b_3$ .

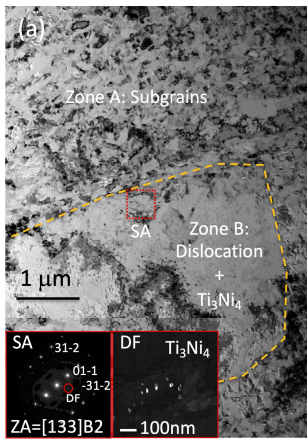
The TEM observations are also performed on the 500°C-annealed sample, to study the starting microstructure and operating deformation mechanism, before and after single tensile deformation. Fig. 10a presents the starting microstructure of 500°C-annealed NiTi. The partial recrystallization

results in two different zones of microstructure: Zone A is composed by subgrains in the size of 100nm; Zone B is composed by dislocations and  $\text{Ti}_3\text{Ni}_4$  precipitates. The precipitates are studied by reorienting the TEM foil to  $[133]\text{B2}$  zone axis in Zone B. The SA diffraction pattern (in the inset of Fig. 10a) shows the reflections of  $\text{Ti}_3\text{Ni}_4$  phase [21]. The ellipsoidal morphology and 20nm size of the precipitates can be seen from the corresponding DF image in the inset of Fig. 10a. BF imaging using dislocation contrast near  $[111]\text{B2}$  zone axis is performed in both Zones A and B. Fig. 10(b) shows the size of a group of subgrains (100nm in diameter) and the sub grain boundaries under  $g=[0-11]\text{B2}$  and  $g=[-110]\text{B2}$  conditions. Neither visible dislocation contrast nor  $\text{Ti}_3\text{Ni}_4$  precipitate is observed in the subgrains. Same observations are performed in Zone B. Individual dislocation lines (Burgers vectors  $b_1=a[001]$ ,  $b_2=a[100]$  and  $b_3=a[010]$  and the axes are marked in the figures by yellow dash lines), rearranging dislocations in sub-GB formation and  $\text{Ti}_3\text{Ni}_4$  precipitate contrast are observed in this zone. The TEM observations are then focused on the 8 wppm H sample (500°C-annealed) after single tensile deformation to  $\epsilon=0.06$ . The micrographs are shown in the Fig. 10d, 10e and 10f for microstructure view, Zone A (subgrains) analysis and Zone B (dislocations and  $\text{Ti}_3\text{Ni}_4$  precipitates), respectively. The dislocation contrast images at Zone A (Fig. 10e) demonstrate parallel straight dislocation lines ( $b_3=[010]$ ) in the subgrains at zone of interest (ZOI is marked by black dash squares). Dislocations of  $b_1=[001]$  and  $b_2=[100]$  are almost absent under favorable imaging conditions. At Zone B, the deformed 8 wppm H-containing sample does not show much differences on dislocation distribution and dislocation density when comparing to non-deformed conditions. In addition, no residual martensite, neither R-phase nor  $\text{B19}'$  phase, is observed in any zone. It suggests the complete reverse transformation after unloading the sample from tensile stress, which is in good agreement with the unloading tensile curve recorded in the cyclic tensile test (Fig. 1b).

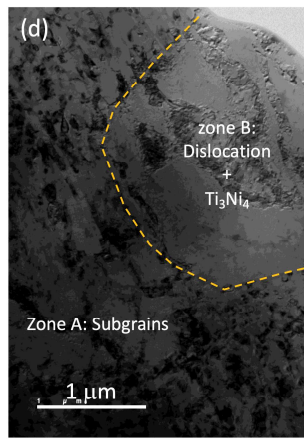
Same TEM observation protocol is applied to the 40 wppm H sample after the same tensile deformation. Fig. 10g, 10h and 10i present the TEM micrographs. The most visible difference seen after comparing to the images of non-deformed sample and 8 wppm H sample is the dislocation activity in Zone B (Fig. 10i). It recalls the similar dislocation microstructure observed in the non-transformed B2 island in the 800°C-annealed samples containing the same concentration of hydrogen. However, because the observations are performed in the deformation samples after unloading (reversion of  $\text{B19}'$  to B2), no conclusive deformation mechanisms can be determined for the 500°C-annealed samples. Yet, the observed changes in the deformation microstructure may suggest a modification of the local deformation mechanism in play.

500°C-annealed microstructure

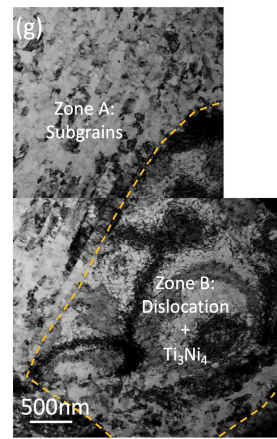
(a) As-annealed  $\epsilon=0$



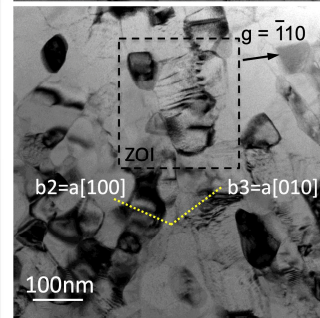
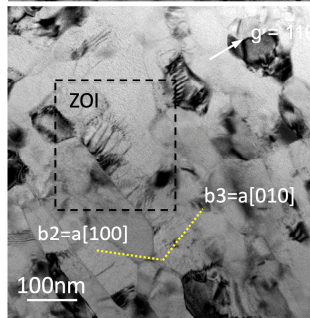
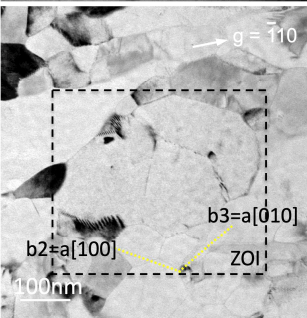
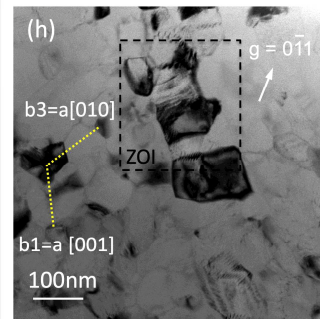
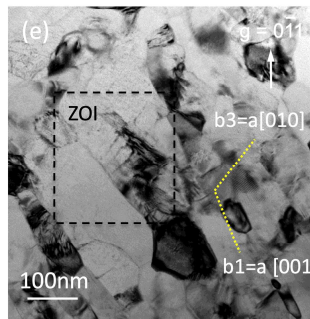
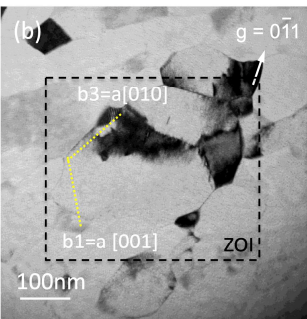
(b) 8 wppm H  $\epsilon=0.06$



(c) 40 wppm H  $\epsilon=0.06$



Subgrain zone



Dislocation +  $Ti_3Ni_4$  zone

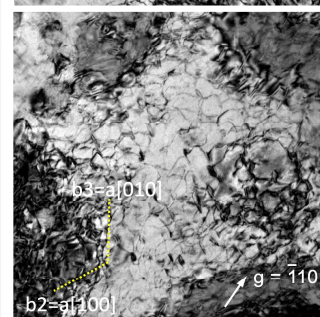
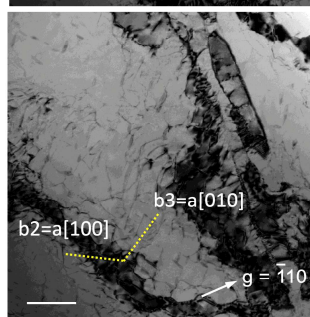
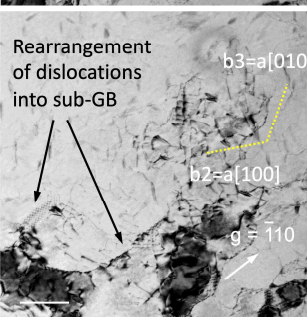
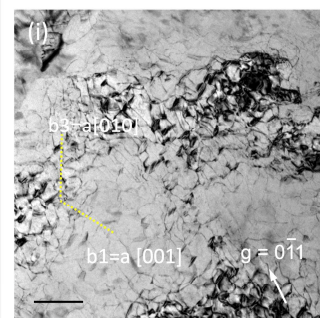
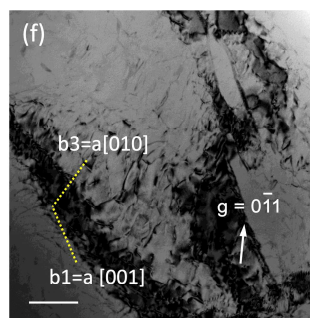
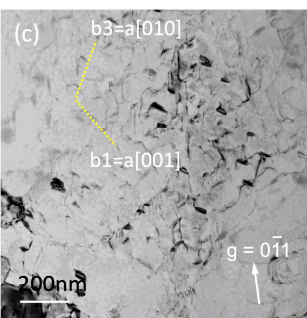


Figure 10: Micrographs of the TEM observation on the microstructure of 500 ° C-annealed samples before and after deformation to  $\epsilon=0.06$ . (a) The BF imaging of the sample at as-500°C-annealed state. Two zones of different microstructures are observed. Zone A: the zone of subgrains of grain size around 100 nm; Zone B: the zone of dislocations and precipitates (marked by orange dash lines, the zone size is about 5  $\mu\text{m}$  in diameter) without subgrain structure. The diffraction pattern (SA at red dash square) is shown in the inset indicating the presence of two  $\text{Ti}_3\text{Ni}_4$  variants in Zone B. The DF image (in the inset) of  $\text{Ti}_3\text{Ni}_4$  precipitates; (b) Zone A is magnified and tilted to dislocation contrast conditions  $g=0-11\text{B}2$  and  $g=-110\text{B}2$ , no visible dislocations are observed; (c) Zone B is magnified and tilted to the same contrast conditions, dislocations ( $b_1=a[001]$ ,  $b_2= a[100]$  and  $b_3=a[010]$ ) can be seen; (d) BF image of the deformation microstructure of the 8 wppm H sample (500 ° C-annealed) after unloading from  $\epsilon=0.1$ ; (e) Dislocation contrast images at  $g=0-11$  and  $g=-110$  in Zone A; (f) Dislocation contrast images at  $g=0-11\text{B}2$  and  $g=-110\text{B}2$  in Zone B; (g) BF image of the deformation microstructure of the 40 wppm H sample (500°C-annealed) after unloading from  $\epsilon=0.1$ ; (h) Dislocation contrast images at  $g=0-11$  and  $g=-110$  in Zone A; (i) Dislocation contrast images at  $g=0-11\text{B}2$  and  $g=-110\text{B}2$  in Zone B. In (b), (e) and (h), zone of interest (ZOI) is marked by black dash square at which the zone axis is used to establish the dislocation contrast.

### 3.4. TDS results and hydrogen redistribution

The TDS thermogram of hydrogen in the stent sample (Stent #4 among the commercial stents mentioned in Table 1) is shown in Fig. 11a. Gaussian peak fitting is used to deconvolute the multiple desorption peaks [30]. The thermogram can be fitted by three Gaussian peaks centered at 617°C, 657°C and 733°C. The peaks at different desorption temperatures are signatures of the hydrogen interaction sites with different binding energies with the matrix. Because the stent sample has been stored at room temperature (RT) for several months before TDS measurement, the diffusion from surface to the core should have been already completed according to the experimental results obtained by Duerig *et al.* [19]. Therefore, a time-dependent redistribution of hydrogen in the NiTi microstructure may be the cause of three desorption peaks. The hydrogen redistribution phenomenon is also observed in the 40 wppm H 800°C-annealed sample during RT aging. Fig. 11b shows the TDS thermogram and Gaussian peak fitting of the 40 wppm H sample after 24 hours RT aging. The 24 hours aging allows about 0.25 mm diffusion depth of hydrogen from surface towards core [19], which corresponds to a “core charging” condition from both surfaces in the 0.5mm-thick plate used in this study. The 24 hours-aged sample displays a symmetrical single peak centered at

652°C, that can be fitted by a single Gaussian type peak (Fig. 11b). It indicates that hydrogen atoms in the material, at this stage, reside in sites with similar bonding-energy. These sites have been proposed to be the pseudo octahedral sites of B2 lattice [19]. After aging at room temperature for 192 hours, the TDS thermogram presents a peak partially shifted towards higher temperatures. The thermogram can be well fitted by three Gaussian type peaks centered at 640°C, 700°C and 754°C. Among them, the main peak is the one centered at 640°C, almost at the same temperature as the peak in the 24 hours-aged sample: it represents 76.4% of the total desorbed H<sub>2</sub>. The other two peaks, at higher temperatures of 700°C and 754°C, represent 15.7% and 7.9% of the total H<sub>2</sub> desorption, respectively. This observed evolution of the TDS thermograms with aging suggests an isothermal hydrogen redistribution can occur in fully recrystallized NiTi at room temperature. Accordingly, it would be reasonable to assume that such room temperature redistribution could also happen in the 500°C-annealed stent. However, possible redistribution sites should be very complex due to the microstructure complexity (Fig. 10a) and will be the subject of further works.

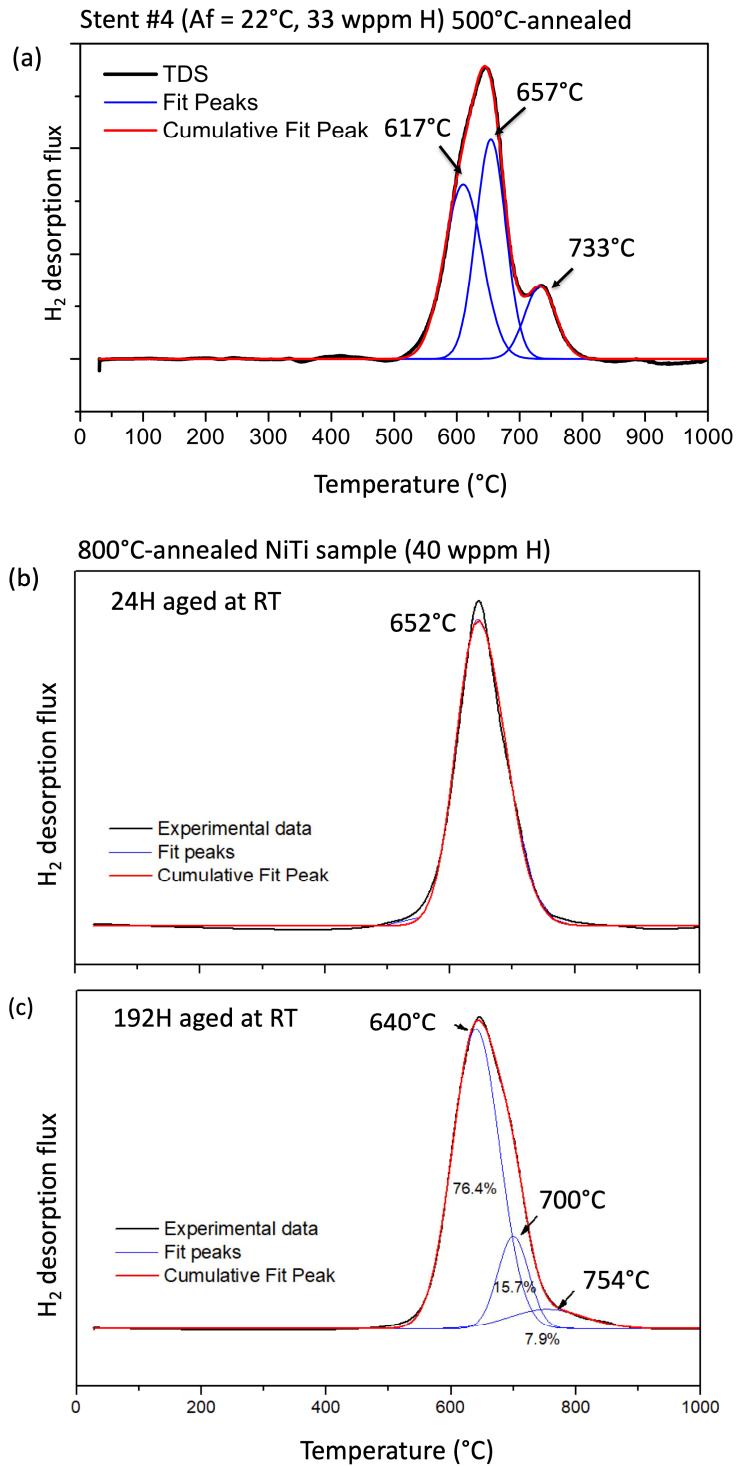


Figure 11. Thermal desorption thermograms of the  $500^\circ\text{C}$ -annealed stent sample (Stent #4) and 40 wppm H hydrogenated  $800^\circ\text{C}$ -annealed NiTi samples. (a)  $500^\circ\text{C}$ -annealed stent sample with 33 wppm H after long-time aging at RT ( $> 1$  month); (b) 40 wppm H  $800^\circ\text{C}$ -annealed sample after 24 hours aging at RT; (c) 40 wppm H  $800^\circ\text{C}$ -annealed sample after 192 hours aging at RT. The experimental data (black line) can be deconvoluted into Gaussian peaks (in blue). In red is the sum of all Gaussian peaks, indicative of correct fit.

## 4. Discussion

### 4.1. Hydrogen effects on the Ms temperature and SIM stress

The hydrogen effects on the martensitic transformation temperatures have been widely studied [7,31–33] and it was previously reported with consistency that the hydrogen content notably reduces the Ms temperature of NiTi. In the 800°C-annealed samples, the Ms temperature of 40 wppm H sample is 10.6°C lower than for 8 wppm H sample, directly impacting the stability level of austenite in the sample with high hydrogen content. Logically this fact may induce a higher onset stress with respect to the martensitic plateau. Correspondingly, the SIM stress of the 40 wppm H sample is increased of about 25% when compared to the annealed sample (no detectable H) and to the 8 wppm H sample. Very similar results have been observed in literature [8], which reports an increase of approximately 60 MPa when comparing a 50 wppm H sample to a sample with 9 wppm H. In the 500°C-annealed samples, a similar increase of the stress plateau and decrease of Ms (R-B19') are observed (Fig. 1). These results corroborate previous findings [12, 19] showing that hydrogen addition leads to an increase of the austenite phase chemical stability. As a matter of fact, the hydrogen solute acts as B2 stabilizer, hence delays the martensitic transformation during both thermal cooling process and mechanical deformation.

### 4.2. Hydrogen redistribution

In NiTi, it has been reported that hydrogen atoms are mobile (diffusion coefficient =  $3.6 \times 10^{-15} \text{ m}^2/\text{s}$  at 25°C [34] at concentrations in the 50–300 wppm range [35]. The TDS results on the room temperature-aged 40 wppm H sample (Fig. 11b and 11c) show a transition from a single site type distribution to a peak separation after 192 hours aging. The increase of the desorption temperature indicates a reduction of the free energy of hydrogen which are trapped in the lattice defects, providing extra binding energy. In the fully recrystallized sample with single B2 phase, the potential trapping sites could probably be grain boundaries. Based on the *in situ* EBSD measurements, the GB characteristics can be obtained in the 800°C-annealed sample (40 wppm H). By assuming that GBs can act as localized trapping sites for hydrogen [36, 37], the GB map (Fig. 11b) is colored for two

groups of grain boundaries according to their interfacial energies  $E_{gb}$  [38] as: Random GBs with  $E_{gb} > 600 \text{ mJ/m}^2$  (blue) and Low energy GBs with  $E_{gb} = 200\text{-}500 \text{ mJ/m}^2$  (red). Among the low energy ones, the energies of  $\Sigma 11(332)$ ,  $\Sigma 13(510)$  and  $\Sigma 13(320)$  coincidence site lattice (CSL) GBs are close to  $500 \text{ mJ/m}^2$ . The lowest energy GBs are  $\Sigma 9(114)$ ,  $\Sigma 3(112)$  and low angle GBs at  $200\text{-}300 \text{ mJ/m}^2$ . Meanwhile, the map of non-transformed islands (Fig. 12b) is shown side by side to the GB energy distribution map. The IPF map is presented along the tensile test axis (RD) to illustrate the grain orientations in the islands in addition to Fig. 6c (along ND). It can be noticed that every B2 island is formed around GBs and triple junctions (Fig. 6 and 12), more specifically where low energy GBs are concentrated (correlation made in the black squares of Fig 12a and 12b). Nevertheless, the image correlation is insufficient to be conclusive to link the B2 islands, GBs and hydrogen redistribution. Therefore, the question keeps open if the formation of B2 island results from hydrogen redistribution, thus local enrichment, at certain GB or at other structural defects.

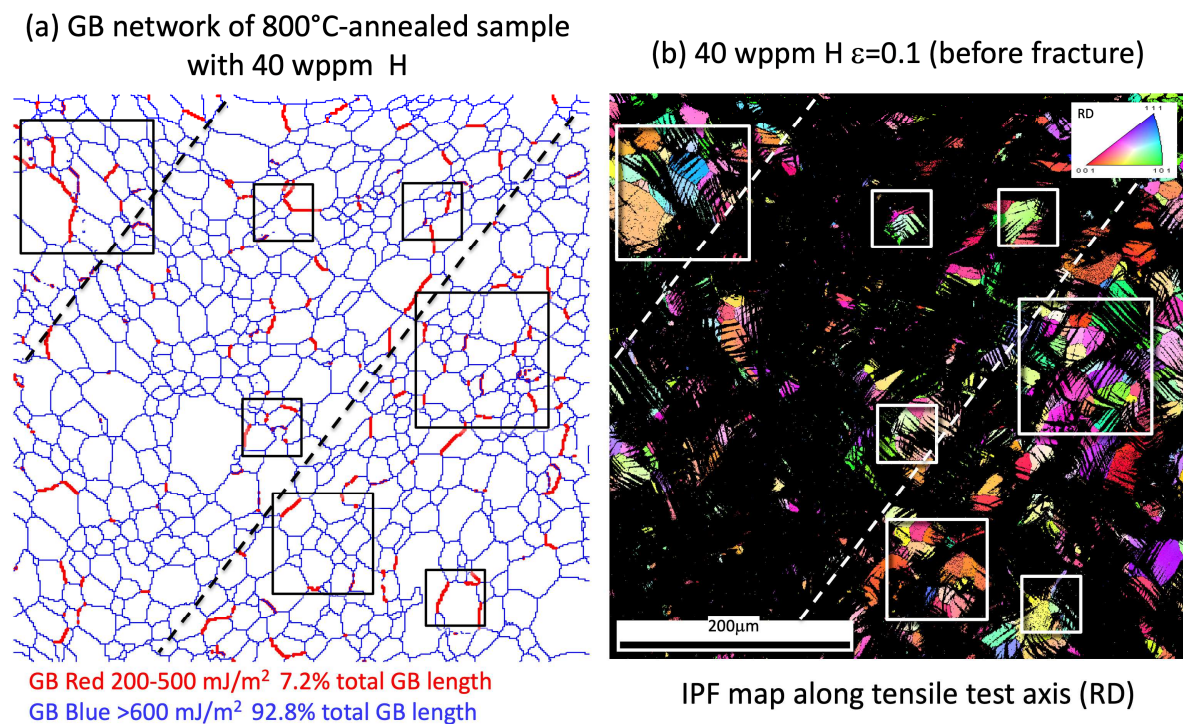


Figure 12: The analysis of the grain orientation and grain boundary (GB) network of the 40 H wppm sample  $\epsilon=0.1$  (before fracture). (a) The distribution of Random GB (in blue, interface energy  $> 600 \text{ mJ/m}^2$ ) and Special GB (in red, interface energy =  $200\text{-}500 \text{ mJ/m}^2$ ); (b) The EBSD IPF map of the non-transformed B2 islands along tensile test axis (RD) of the same map of Fig. 6c. Same squares are marked in each image to help compare the positions of the islands and the nearby GBs. It can be seen

*that each B2 island is formed around GB and GB junctions. The band-like microstructure is delimited by dash lines in each diagram.*

Despite this, it is known that the hydrogen trapping at grain boundaries and dislocations eventually leads to the decrease of overall ductility in metallic alloys [35]. When considering the 500°C-annealed NiTi, the interpretation of TDS thermogram (Fig. 11a) by hydrogen trapping would be complicated due to the complexity of the partially recrystallized structure. The structural defects, such as sub-GBs, dislocations,  $Ti_3Ni_4$  precipitates, can serve as potential trapping sites as reported in the steels (ref 28). Moreover, the situation can be more complicated since the subgrains and dislocations/ $Ti_3Ni_4$  precipitates are distributed heterogeneously in distinct microstructure zones (Zone A and Zone B shown in Fig. 10). Furthermore, by considering the time-dependent nature of the trapping process, an “incubation” period exists, during which the hydrogen diffuses firstly from surface to the core then redistributes in the microstructure. The phenomena of progressive loss of ductility after hydrogen-charging has been reported [19], confirming the incubation period of the H impact to the mechanical properties of NiTi. Such incubation further increases the danger of H uptake/amount in stents, because the quality inspection is usually performed soon after the stent surface treatment.

#### **4.3. Change of the local deformation mechanism in 800°C-annealed NiTi**

The results of in-situ and ex-situ observations of the operating deformation mechanism indicate the tendency of the local promotion of dislocation slip in the 40 wppm hydrogen-charged samples, in both partially and fully recrystallized microstructures. Taking the fully recrystallized sample for analysis, it is pointed out that the slope of the stress-strain curve beyond the plateau (Fig. 7b) is higher (+3 GPa) and the plastic deformation of martensite starts at higher stress in 40 wppm H sample. This suggests that the plastic deformation of the stress induced martensite phase could be partially suppressed at both mesoscopic and microscopic scales. The contrast of the slope is thought to originate from the differences of the microstructural evolution. That could be due to the change of local deformation mechanism at mesoscopic scale. The B2 matrix almost fully transforms into

martensitic phase B19' at the end of superelastic regime in the 8 wppm H sample after the propagation of MBF. In contrast, the SIM in 40 wppm H sample seems concentrated in the MB, the propagation of which seems interrupted until fracture ( $\epsilon = 0.1$ ). Such mesoscale localization of strain in annealed NiTi has been reported [26] but the presence of hydrogen seems to affect it by the formation of non-transformed B2 islands. These B2 islands form in 40 wppm H sample both inside and outside the mesoscopic band microstructure leading to a mixture of 85% martensite and 15% non-transformed B2 when passing to the plastic regime. From microscopic point of view, the dislocation slip is promoted in the B2 islands. By gathering all the observations, there seems to be a two-fold effect of the absorbed hydrogen on the localization of macroscopic deformation as well as on the localization of deformation on individual grains. Nevertheless, it is difficult to determine the relationship between the B2 islands and the interruption of MB propagation since EBSD results are not sufficient to measure the localization of mesoscale deformation. What can be suggested is that, in the 40 wppm H sample (800°C-annealed), the heterogeneous deformation happens during the superelastic-plastic transition as a result of deformation contrasts at MB and its surrounding, and at slip dominant non-transformed B2 islands and their environs. Such heterogeneous deformation is usually associated with strong macroscopic strengthening effect due to microscopic stress concentration [39]. The strengthening effect is observed in the 40 wppm H sample (800°C-annealed) that the plateau stress increases more rapidly than that in 8 wppm H sample (800°C-annealed) (Fig. 7b). About the hydrogen's effect to the localization of dislocation slip, a theory called Hydrogen-Enhanced Localized Plasticity (HELP) is worth mentioned to explain enhanced tendency for localization of dislocation slip in the non-transformed B2 islands due to the absorbed hydrogen, similar to many hydrogen-charged alloys near stress concentrations areas, e.g. crack tips [40].

#### **4.4. Partially recrystallized NiTi used in stent application and the effect of hydrogen**

The microstructure used in NiTi for stent application is partially recrystallized from as-drawn raw material. The structural defects in the raw material, i.e. high density of dislocations, are partially recovered through annihilation and rearrangement to form subgrain structure during the thermomechanical treatments. The treatment is performed at intermediate temperature, much

inferior to the recrystallization temperature, for limited duration and under geometrical constrain. The treatment is called “shape-setting” to fix the stent geometry via the subgrain formation and to adjust the  $A_f$  temperature. The mechanical properties of NiTi in wide microstructure ranges have been well-studied by Y. Chen et al. [23], showing that the stability of the cyclic superelastic deformation is of high sensitivity to the microstructure and dislocation activities. Moreover, the deformation is concentrated on the mesoscopic scale since the profile of the stent strut is in the dimensions of  $100\mu\text{m}$ . Therefore, the subtle balance between shape-setting and  $A_f$  adjustment is of great importance for performance of the stent in the scope of complete self-expansion and suitable radial force. Thus, the presence of hydrogen in such highly complex microstructure (Fig. 10) adds extra variables which drastically increase the difficulty of accurate control of the deformation behaviors of stent.

In this study, due to the difficulty of applying in-situ EBSD characterization on the  $500^\circ\text{C}$ -annealed NiTi, much less information of the deformation mechanism can be obtained to directly evidence the mesoscopic mechanism change by hydrogen. The changes in microstructures, i.e. the fracture surface (Fig. 1b and 1c) and local dislocation density (Fig. 10), observed under ex-situ conditions (after fracture or after unloading the strained sample) might imply a local change of deformation mechanisms between 8 wppm and 40 wppm hydrogen. Further investigations with suitable in-situ techniques (e.x. Digital Image Correlation DIC) are required to clarify the mesoscopic strain-stress concentration and potentially the change of deformation mechanism of H-charged NiTi with partial recrystallization structure. Nonetheless, the impact of 40 wppm H to the  $500^\circ\text{C}$ -annealed NiTi leads to the same ductility loss (Fig. 1b), similar suppression of martensite transformation (Fig. 1a) and promotion of dislocation activity in specific region of the microstructure (Fig. 10c) as observed in  $800^\circ\text{C}$ -annealed NiTi. The fact raises the concern about the structural damage of hydrogen containing NiTi stent undergoing the crimping process.

## 5. Conclusion

The present work revisits the effects of low-concentration hydrogen on mechanical properties of NiTi materials, with regards to hydrogen contents found in commercial stents (6 to 55 wppm). Two

hydrogen concentrations, 8 wppm and 40 wppm, are therefore studied in both 500°C-annealed NiTi and 800°C-annealed NiTi to illustrate the hydrogen influences to the mechanical property and deformation mechanism of NiTi. The results present that, after aging 192 hours at room temperature, the presence of 40 wppm hydrogen reduces drastically the ductility of NiTi with an observable increasing of onset stress of SIM in both 500°C-annealed NiTi and 800°C-annealed NiTi. In the 8 wppm H sample, the mechanical property does not exhibit significant changes. In-situ EBSD coupled with tensile loading and ex-situ TEM observations detect the local changes of operating deformation mechanisms. In the 800°C-annealed samples, 40 wppm H leads to interruption of MB propagation and the formation of non-transformed B2 islands (14.8 area%) during the superelastic deformation. In the 500°C-annealed sample, 40 wppm H leads to extensive dislocation activity at the microstructural zones containing dislocations and  $Ti_3Ni_4$  precipitates. TDS confirms that a hydrogen redistribution has happened in the 40 wppm hydrogen during the homogenization process. The mesoscale MB propagation, the formation of the non-transformed B2 islands and the microscale change of deformation mechanism are discussed in relation to the redistribution of the hydrogen. For stent safety, extensive attentions should be paid to the low-concentration hydrogen absorption during stent manufacturing in order to minimize the risk of hydrogen related issues (high radial stress, strut fracture during crimping, incomplete self-expansion, etc.).

### **Acknowledgement**

The authors acknowledge the research collaboration between the team of Métallurgie Structurale IRCP and the team of Laboratoire d'Etude de la Corrosion Aqueuse, CEA Saclay, supported by the Métallurgie Structurale IRCP. The authors acknowledge the great help from Dr. Domitille GIAUME in the collaboration and the discussions with Dr. Philippe VERMAUT about the crystallography of martensitic phase transformation in the shape memory alloys and the techniques for TEM observations.

### **References**

- [1] N.B. Morgan, Medical shape memory alloy applications - The market and its products, Mater. Sci. Eng. A. 378 (2004) 16–23. doi:10.1016/j.msea.2003.10.326.

- [2] Y. Zheng, X. Xu, Z. Xu, J.Q. Wang, H. Cai, *Metallic Biomaterials: new directions and Technologies.*, first ed., Wiley-VCH, Weinheim, Germany 2017.
- [3] T. Duerig, A. Pelton, D. Sto, An overview of nitinol medical applications, *Mater. Sci. Eng. A*. 275 (1999) 149–160. doi:10.1016/S0921-5093(99)00294-4.
- [4] G. Mani, M.D. Feldman, D. Patel, C.M. Agrawal, Coronary stents: A materials perspective, *Biomaterials*. 28 (2007) 1689–1710. doi:10.1016/j.biomaterials.2006.11.042.
- [5] F. Sun, L. Jordan, V. Albin, V. Lair, A. Ringuedé, F. Prima, On the high sensitivity of corrosion resistance of NiTi stents with respect to inclusions: an experimental evidence, *ACS Omega*. 5 (2020) 3073-3079. doi:10.1021/acsomega.9b04312.
- [6] ASTM F86, Standard Practice for Surface Preparation and Marking of Metallic Surgical, Practice. 04 (2011) 2009–2011. doi:10.1520/F0086-04R09.2.
- [7] J. Sheriff, A.R. Pelton, L.A. Pruitt, Hydrogen effects on nitinol fatigue. In: Proceedings of the ASM symposium on materials and processes for medical devices conference, Boston, MA, 13–16 November, (2005) pp. 38–43. Materials Park, OH : ASM International.
- [8] R. Sarraj, T. Hassine, F. Gamaoun, Mechanical behavior of NiTi arc wires under pseudoelastic cycling and cathodically hydrogen charging Mechanical behavior of NiTi arc wires under pseudoelastic cycling and cathodically hydrogen charging, *Mater. Res. Express*. 5(1) (2018) id 015704. doi:10.1088/2053-1591/aa9f02.
- [9] A. Runciman, K.C. Chen, A.R. Pelton, C. Trépanier, Effects of Hydrogen on the Phases and Transition Temperatures of NiTi, (2008) 185–195. doi:10.1361/cp2006smst185.
- [10] W. Elkhail Letaief, T. Hassine, F. Gamaoun, Tensile behaviour of superelastic NiTi alloys charged with hydrogen under applied strain, *Mater. Sci. Technol. (United Kingdom)*. 33 (2017) 1533–1538. doi:10.1080/02670836.2017.1320084.
- [11] S.W. Robertson, On the Mechanical Properties and Microstructure of Nitinol for Biomedical Stent Applications, PhD Thesis (2006) University of California, Berkeley.
- [12] T. Asaoka, Effect of Hydrogen on Martensite Phase Deformation in Ti-Ni Shape Memory Alloy, *J. Soc. Mat. Sci. Japan*. 41(470) (1992) 1630-1635. doi:10.2472/jsms.41.1630.
- [13] M. Rokbani, L. Saint-Sulpice, S.A. Chirani, T. Bouraoui, Hydrogen effects on Ni-Ti fatigue performance by self -heating method, *Smart Mater. Struct.* 26(10) (2017). doi:10.1088/1361-665X/aa86f4.

- [14] F. Gamaoun, M. Ltaief, T. Bouraoui, Effect of hydrogen on the tensile strength of aged Ni – Ti superelastic alloy, 22 (2011) 2053–2059. doi:10.1177/1045389X11423427.
- [15] K. Yokoyama, T. Ogawa, K. Takashima, K. Asaoka, J. Sakai, Hydrogen embrittlement of Ni-Ti superelastic alloy aged at room temperature after hydrogen charging, Mater. Sci. Eng. A. 466 (2007) 106–113. doi:10.1016/j.msea.2007.02.102.
- [16] K. Yokoyama, M. Tomita, J. Sakai, Hydrogen embrittlement behavior induced by dynamic martensite transformation of Ni-Ti superelastic alloy, Acta Mater. 57 (2009) 1875–1885. doi:10.1016/j.actamat.2008.12.030.
- [17] T. Ogawa, T. Oda, K. Maruoka, J. Sakai, Effect of aging at room temperature on hydrogen embrittlement behavior of Ni-Ti superelastic alloy immersed in acidic fluoride solution, Int. J. Mech. Mater. Eng. 10 (2015). doi:10.1186/s40712-015-0039-6.
- [18] K. Asaoka, K. Yokoyama, M. Nagumo, Hydrogen Embrittlement of Nickel-Titanium Alloy in Biological Environment, Metal. Mater. Trans. A. 2002;33:495–501. doi:10.1007/s11661-002-0111-8.33 (2002) 495–501.
- [19] T. Duerig, O. Shelley, D. Madamba, L. Vien, A Practitioner’s Perspective of Hydrogen in Ni-Ti Alloys, Shape Mem. Superelasticity. 5 (2019) 235–248. doi:10.1007/s40830-019-00225-6.
- [20] F 2063 – 05, Standard Specification for Wrought Nickel-Titanium Shape Memory Alloys for Medical Devices and Surgical Implants, Annu. B. ASTM Stand. (2012) 1–6. doi:10.1520/D2063.
- [21] K. Otsuka, X. Ren, Physical metallurgy of Ti-Ni-based shape memory alloys, Prog. Mater. Sci. 50 (2005) 511–678. doi:10.1016/j.pmatsci.2004.10.001.
- [22] K. Otsuka, C.M. Wayman, Shape Memory Materials, Cambridge University Press, 1998.
- [23] Y. Chen, O. Tyc, O. Molnárová, L. Heller, P. Šittner, Tensile Deformation of Superelastic NiTi Wires in Wide Temperature and Microstructure Ranges, Shape Mem. Superelasticity. 5 (2019) 42–62. doi:10.1007/s40830-018-00205-2.
- [24] P. Sedmák, J. Pilch, L. Heller, J. Kopeček, J. Wright, P. Sedlák, M. Frost, P. Šittner, Grain-resolved analysis of localized deformation in nickel-titanium wire under tensile load, Science. 353 (2016) 559–562. doi:10.1126/science.aad6700.
- [25] L. Heller, P. Šittner, P. Sedlák, H. Seiner, O. Tyc, L. Kadeřávek, P. Sedmák, M. Vronka, Beyond the strain recoverability of martensitic transformation in NiTi, Int. J. Plast. (2019). doi:10.1016/j.ijplas.2019.01.007.

- [26] Y. Chen, O. Molnárová, O. Tyc, L. Kadeřávek, L. Heller, P. Šittner, Recoverability of large strains and deformation twinning in martensite during tensile deformation of NiTi shape memory alloy polycrystals, *Acta Mater.* 180 (2019) 243–259. doi:10.1016/j.actamat.2019.09.012.
- [27] E. Polatidis, M. Šmíd, I. Kuběna, W.N. Hsu, G. Laplanche, H. Van Swygenhoven, Deformation mechanisms in a superelastic NiTi alloy: An in-situ high resolution digital image correlation study, *Mater. Des.* 191 (2020) 1–10. doi:10.1016/j.matdes.2020.108622.].
- [28] T. Simon, A. Kröger, C. Somsen, A. Dlouhy, G. Eggeler, On the multiplication of dislocations during martensitic transformations in NiTi shape memory alloys, *Acta Mater.* 58 (2010) 1850–1860. doi:10.1016/j.actamat.2009.11.028.
- [29] L. Dong, R.H. Zhou, X.L. Wang, G.K. Hu, Q.P. Sun, On interfacial energy of macroscopic domains in polycrystalline NiTi shape memory alloys, *Int. J. Solids Struct.* 80 (2016) 445–455. doi:10.1016/j.ijsolstr.2015.10.006.
- [30] W. Lisowski, E.G. Keim, A.H.J. Van Den Berg, M.A. Smithers, Thermal desorption of deuterium from modified carbon nanotubes and its correlation to the microstructure, *Carbon N. Y.* 44 (2006) 974–982. doi:10.1016/j.carbon.2005.10.007.
- [31] M. Tomita, K. Yokoyama, K. Asaoka, J. Sakai, Hydrogen thermal desorption behavior of Ni-Ti superelastic alloy subjected to tensile deformation after hydrogen charging, *Mater. Sci. Eng. A.* 476 (2008) 308–315. doi:10.1016/j.msea.2007.04.104.
- [32] Y. Adachi, Effect of Hydrogen on the Shape Memory Effect and Transformation Behavior of Ti-Ni Alloy, (2015). doi:10.2320/jinstmet1952.54.5.
- [33] S.C. Mao, X.D. Han, Y.B. Tian, J.F. Luo, Z. Zhang, Y. Ji, M.H. Wu, In situ EBSD investigations of the asymmetric stress-induced martensitic transformation in TiNi shape memory alloys under bending, *Mater. Sci. Eng. A.* 498 (2008) 278–282. doi:10.1016/j.msea.2008.07.072.
- [34] R. Schmidt, M. Schlereth, H. Wipf, W. Assmus, M. Müllner, Hydrogen solubility and diffusion in the shape-memory alloy NiTi, *J. Phys. Condens. Matter* 1 (1989) 2473. doi:10.1088/0953-8984/1/14/003
- [35] A. Moitra, K.N. Solanki, M.F. Horstemeyer, The location of atomic hydrogen in NiTi alloy: A first principles study, *Comput. Mater. Sci.* 50 (2011) 820–823. doi:10.1016/j.commatsci.2010.10.013.

- [36] Y.S. Chen, H. Lu, J. Liang, A. Rosenthal, H. Liu, G. Sneddon, I. McCarroll, Z. Zhao, W. Li, A. Guo, J.M. Cairney, Observation of hydrogen trapping at dislocations, grain boundaries, and precipitates, *Science* 367 (2020) 171-175. doi:10.1126/science.aaz0122.
- [37] M. Aucouturier, Grain boundary segregations and hydrogen embrittlement, *Journal de Physique Colloques* 43(C6) (1982) 175-186. doi:10.1051/jphyscol:1982617.jpa-00222298.
- [38] F. Yazdandoost, R. Mirzaeifar, Tilt grain boundaries energy and structure in NiTi alloys, *Comput. Mater. Sci.* 131 (2017) 108–119. doi:10.1016/j.commatsci.2017.01.027.
- [39] Y. Zhu, X. Wu, Perspective on hetero-deformation induced (HDI) hardening and back stress, *Mater. Res. Lett.* 7 (2019) 393–398. doi:10.1080/21663831.2019.1616331.
- [40] H.K. Birnbaum, P. Sofronis, Hydrogen-enhanced localized plasticity-a mechanism for hydrogen-related fracture, *Mater. Sci. Eng. A.* 176 (1994) 191–202. doi:org/10.1016/0921-5093(94)90975-X.